



DESIGN AND DEVELOPMENT OF AN EEG-BASED BRAIN COMPUTER INTERFACE (BCI) SYSTEM

Graduation Project Report

submitted in partial fulfillment of the requirements for the

Bachelor of the Science of Engineering Honors Degree

To

The Department of Electrical and Telecommunication Engineering

Faculty of Engineering
South Eastern University of Sri Lanka
University Park, Oluvil, #32360
Sri Lanka

by

M.W.V.C. MANAWEERA (SEU/IS/18/EG/025)

K.P. WIJESIGHE (SEU/IS/18/EG/029)

Supervised by:

Eng. Hirshan Rajendran

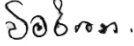
Dr. M.N.A. Hinas


Dr. W.G.C.W. Kumara

17 September 2024

DECLARATION

We hereby declare that this project report is based on our original work except for citations and quotations which have been duly acknowledged. We also declare that it has not been previously and concurrently submitted for any other degree or award at South Eastern University of Sri Lanka or other institutions.

Signature : 
Name : M.W.V.C Manaweera
REG No. : SEU/IS/18/EG/025
Date : 17 September 2024

Signature : 
Name : K.P. Wijesinghe
REG No. : SEU/IS/18/EG/029
Date : 17 September 2024

APPROVAL

We certify that this project report entitled “DESIGN AND DEVELOPMENT OF AN EEG-BASED BRAIN COMPUTER INTERFACE (BCI) SYSTEM” was prepared by M.W.V.C Manaweera, KP Wijesinghe has met the requirement standard for submission for the degree of B.Sc. Engineering (Hons) at South Eastern University of Sri Lanka.

Approved by,

Signature : _____

Supervisor : Eng. Hirshan Rajendran

Date : _____

Signature : _____

Co-Supervisor : Dr. M.N.A. Hinas

Date : _____

Signature : _____

Co-Supervisor : Dr. W.G.C.W. Kumara

Date : _____

ACKNOWLEDGEMENTS

We are pleased to acknowledge the invaluable support from the Department of Electrical and Telecommunication Engineering, without which the success of our project would not have been possible. Many individuals have contributed significantly to the progress of our work, and we are deeply grateful to all who have supported us throughout this journey.

Firstly, we extend our heartfelt gratitude to our primary supervisor, Eng. Hirshan Rajendran, for his insightful guidance, practical advice, and innovative ideas, which have been instrumental in the successful completion of our project. His constant support and expertise have been invaluable to our progress.

We would also like to express our sincere appreciation to Dr. M.N.A. Hinas and Dr. W.G.C.W. Kumara for their comprehensive support in the technical aspects of our project. Their expertise and encouragement were critical to our success.

Furthermore, we are grateful to the staff members of the Department of Electrical and Telecommunication Engineering for their unwavering assistance and contributions.

ABSTRACT

This project focuses on the design and development of an EEG-based Brain-Computer Interface (BCI) system, aimed at providing a low-cost solution for disabled individuals to communicate and control devices using Steady-State Visual Evoked Potentials (SSVEP).

The system captures EEG signals via a single-channel setup with three electrodes, amplifies and processes the signals to remove noise and artifacts, and extracts features using the Fast Fourier Transform (FFT). These features, corresponding to distinct flickering frequencies (13 Hz, 17 Hz, and 21 Hz), are classified using a Convolutional Neural Network (CNN) model.

The system's enables real-time interaction with external devices based on the user's focus on specific flickering stimuli. Results from testing the system on publicly available EEG datasets confirm its effectiveness in detecting SSVEP-based signals and accurately controlling external devices. This project presents an affordable alternative to existing expensive systems, contributing to assistive technology for individuals with severe disabilities.

Key results include successful signal acquisition, processing, and classification, along with a well-integrated software interface, showcasing the system's potential for real-world applications in home automation and other assistive technologies.

Table Of Contents

DECLARATION	2
APPROVAL.....	3
ACKNOWLEDGEMENTS	4
ABSTRACT.....	5
LIST OF FIGURES	8
1. INTRODUCTION.....	11
1.1 BACKGROUND.....	11
1.2 AIM AND OBJECTIVES	11
2. LITERATURE REVIEW	13
2.1 EXISTING WORK	13
2.1.1 Current Human-Computer Interfaces	13
2.1.1.1 Brain-Computer Interface.....	13
2.2 THEORY BEHIND THE PROPOSED DEVICE.....	16
2.2.1 Electroencephalography.....	16
2.2.2 Biopotential Electrodes	17
2.2.3 Steady-State Visually Evoked Potentials	18
2.2.4 EEG Frequency Bands	20
2.2.5 Noise and Interference During Measurement	20
2.2.6 EEG Measurement Circuit	21
2.2.7 Feature Extraction and Probability Distributions	24
3. METHODOLOGY.....	27
3.1 SIGNAL ACQUISITION	28
3.1.1 Circuit Design	28
3.1.2 Protection Circuit	30
3.1.3 Instrumentation Amplifier.....	31
3.1.4 Gain Stage and Alias Filter	33

3.1.5	Gain Stage and Alias Filter	Error! Bookmark not defined.
3.1.6	CMRR of Circuit	36
3.1.7	Frequency Response of the Circuit	37
3.2	SIGNAL PROCESSING	45
3.3	FEATURE EXTRACTION	47
3.4	CLASSIFIER DESIGN	48
3.5	USER INTERFACE AND SOFTWARE DESIGN	49
4.	RESULTS	52
4.1	SIGNAL ACQUISITION	52
4.2	SIGNAL PROCESSING	61
4.3	FEATURE EXTRACTION	62
4.4	CLASSIFIER DESIGN	63
4.5	USER INTERFACE AND SOFTWARE DESIGN	65
5.	DISCUSSION	67
6.	CONCLUSION	69
7.	REFERENCES	70

LIST OF FIGURES

Figure 1 illustrates an example of stimulation frequency arrangements, showing 30 frequencies ranging from 5 Hz to 7.9 Hz, spaced at 0.1 Hz intervals, based on the work of H. Han-Jeong et al. [19].....	14
Figure 2: The 10-20 electrode placement system, shown from the (A) left side and (B) top view of the head – Image from J. Malmivuo and R. Plonsey [11].	16
Figure 3: (a) Bipolar electrode placement (O2-O1). (b) Unipolar electrode placement (Oz-left ear)	17
Figure 4 (a) Wet EEG cup electrodes - Images from Kandel Medical [21]. (b) Dry EEG electrodes - Image from Guger Technologies [22]	17
Figure 5: Figure 8 Different areas of the brain – Image from the Mayfield Clinic[1].	18
Figure 6: : (Blue) Frequency spectrum of EEG without stimulus. (Red) Frequency spectrum of EEG with 15Hz stimulus showing 2nd and 3rd harmonics – Image From L. Maciej et al. [28]. .	19
Figure 7: EEG frequency bands and their corresponding mental states – Image from M.G.N. Garcia et al. [2].....	20
Figure 8:Example protection circuit – Image from B. Fong et al [34]	22
Figure 9:Biomeasurement circuit utilising a driven right leg circuit.....	23
Figure 10: : Two representative histograms of the envelope and probability distributions (blue line: log-normal distribution; red: gamma distribution; green: Rayleigh distribution) for preterm EEGs. (a) An example of a probability distribution well-fitted by a log-normal distribution, with data obtained from an infant at a postconceptional age of 32 weeks. (b) An example of a probability distribution well-fitted by a gamma distribution, with data obtained from an infant at a postconceptional age of 44 weeks – Image from R. Saji et al. [40].	25
Figure 11: Overview of the System Functionality for an EEG-Based Brain-Computer Interface (BCI) System	27
Figure 12: Block diagram of EEG measurement circuit connected to the user	29
Figure 13:Circuit diagram of the protection circuit . VElectrode is the input from the positive and negative electrode. VProct is the positive and negative output of the protection circuit	30
Figure 14: (a) Input (yellow) and output (blue) of protection circuit from input within the normal operating range. (b) Input (yellow) and output (blue) of protection circuit from input outside the normal operating range.....	31
Figure 15: Circuit diagram of the instrumentation amplifier. VProct is the positive and negative output from the protection circuit. Vcm is the common mode voltage measured by the in-amp. Vin-amp is the output of the in-amp. Vref is the 1.5 V reference voltage	32

Figure 16: Circuit diagram for gain stage and alias filter. Vin-amp is the output of the in-amp. Vadc_A0 is the output of the alias filter connected to analog pin A0 on the on the future selected development board (ADS1115).....	34
Figure 17: Circuit diagram for the driven right leg. Vcm is the common mode voltage measured by the in-amp. VDRL_Electrode3 is the output of the DRL connected to the third electrode. Vref is the 1.5 V reference voltage	35
Figure 18:(a) Bitscope Micros ground connected to Vref, generating a differential signal into protection circuit. (b) Bitscope Micros ground connected to DRL, generating a differential signal – Image adapted from Amazon [45]	36
Figure 19:(a) Bitscope Micros ground connected to Vref, generating a common mode signal into protection circuit. (b) Bitscope Micros ground connected to DRL, generating a common signal into protection circuit – Image adapted from Amazon [45]	37
Figure 20:Figure 20:Frequency response of circuit output (simulated and measured)	38
Figure 21: Frequency response of DRL (simulated and measured)	39
Figure 22: Example of a CNN Model Architecture.	48
Figure 23: Block Diagram of the System Structure	50
Figure 24: Simulated frequency response of circuit output from a differential input of 50 μ V	52
Figure 25: Simulated frequency response of driven right leg from a common mode input of 200 mV	52
Figure 26: LTspice EEG measurement circuit diagram	53
Figure 27: An Example of an EEG raw and Filtered Signal Based on a 13 Hz Stimulus.....	61
Figure 28:An Example of FFT Spectrum of filtered signal based on a 13 Hz Stimulus.....	62
Figure 29:An Example of FFT Spectrum of filtered signal based on a 17 Hz Stimulus.....	62
Figure 30: An Example of FFT Spectrum of filtered signal based on a 21 Hz Stimulus.....	63
Figure 31: Confusion Matrix of the CNN model	64
Figure 32: Classification report of the CNN model	64
Figure 33:BCI interface	65
Figure 34: Signal Processing Interface	65
Figure 35: Filtered signal displayed by the software.....	66
Figure 36:The classification of the signal displayed by the software.....	66
Figure 37: FFT Spectrum displayed by the software	66

Table of Tables

Table 1 Table of theoretical input voltage specifications for the circuit	18
Table 2 CMRR of the circuit without the DRL and with the DRL at 10 Hz, 50 Hz and 100 Hz.....	24

Table of Tables

Acronym	Definition
ADC	Analog-to-digital converter
BCI	Brain-computer interface
CMRR	Common mode rejection ratio
DRL	Driven right leg
EEG	Electroencephalography
FFT	Fast Fourier Transform
In-amp	Instrumentation amplifier
MLE	Maximum likelihood estimate
PDF	Probability density function
SSVEP	Steady-state visually evoked potentials

1. INTRODUCTION

1.1 BACKGROUND

Electroencephalography (EEG) was first recorded in 1924 [3] and has since been widely researched, particularly in clinical settings. However, the use of EEG in non-medical and consumer applications, such as brain-computer interfaces (BCIs), has only become more common in recent years [4]. Commercial EEG systems vary significantly in price, ranging from \$100 to \$1,000 for consumer-grade headsets, while high-end clinical systems can cost over \$25,000 [5]. Even the lower-end costs can be prohibitive for many hobbyists and members of the maker community who are interested in exploring EEG technology.

Projects such as OpenEEG provide open-source EEG hardware solutions, estimating a build cost of \$200-\$400 for their “ModularEEG” system [6]. Another open-source hardware provider, OpenBCI, offers its cheapest EEG hardware at \$199 [7]. Despite these efforts, the relatively high cost of these systems continues to pose a barrier for widespread adoption and experimentation within the community.

Open-source hardware and software offer a unique advantage by providing users with the flexibility to modify and enhance systems without being limited by the commercial priorities of proprietary systems [8, 9]. This flexibility can lead to significant innovations, as developers can tailor the technology to their specific needs and interests.

BCIs are a relatively newer technology compared to general-purpose EEG systems and were initially developed as assistive devices for individuals with disabilities. More recently, they have been utilized by able-bodied individuals for various applications, such as gaming and other interactive activities [10]. By making EEG measurement systems and BCI software more accessible through low-cost, open-source designs, this project aims to drive innovation and encourage the development of new applications in the field of brain-computer interfaces.

1.2 AIM AND OBJECTIVES

The main aim of this project is to develop and test a low-cost, EEG-based Brain-Computer Interface (BCI) system that can stimulate, measure, and respond to specific EEG signals, particularly steady-state visually evoked potentials (SSVEP). Since EEG signals are typically in the microvolt range [11], the circuit must effectively isolate these signals from various types of interference that can distort or obscure the readings.

To make this technology accessible, the total cost of the entire system is targeted at around €50, which is half the price of the most affordable commercial EEG headset available online [5]. Additionally, the project aims to create a flexible EEG measurement circuit capable of not only measuring SSVEPs in the 5–20 Hz range but also other biopotentials such as electrocardiography (ECG), electrooculography (EOG), and electromyography (EMG). This adaptability transforms the circuit into a versatile bio amplifier with minor modifications.

The software component of this project will stimulate SSVEPs in users that can be detected by the circuit. Users will be presented with multiple SSVEP stimuli to facilitate choices and navigation within the BCI system. The software must detect the presence of an SSVEP at predefined stimulus frequencies in real-time and respond appropriately. A statistical method will be developed to estimate the likelihood that the user is focusing on a specific stimulus.

Finally, the project aims to disseminate the hardware designs and software source code online under an open-source license, providing a reference for others to learn from, modify, and build upon.

In summary, the specific objectives of the project are to:

- Design and construct a low-cost EEG recording system.
- Develop a flexible BCI system capable of stimulating and detecting SSVEPs.
- Create a statistical method for real-time SSVEP detection.

2. LITERATURE REVIEW

2.1 EXISTING WORK

2.1.1 Current Human-Computer Interfaces

Human-computer interfaces (HCIs) are systems, both hardware and software, that take inputs from a human user and convert them into actions through software. This term covers a wide variety of technologies, but here, we're focusing on existing or proposed HCIs that are controlled by the user's brain activity.

2.1.1.1 Brain-Computer Interface

Brain-computer interfaces (BCIs) are systems that allow communication between a user and a computer through their brain activity. There are different types of BCIs, each using different methods to monitor brain activity:

- EEG-based, such as this project.
- Magnetoencephalography (MEG) based.
- Electrocorticography (ECoG) based.
- Functional magnetic resonance imaging (fMRI) based.
- Near-infrared spectroscopy (NIRS) based.

EEG is a non-invasive method that records the brain's electrical activity using electrodes placed on the scalp. A more detailed exploration of EEG will be provided in a subsequent section. In contrast, ECoG is an invasive technique that involves placing electrodes directly on the brain's surface to measure its electrical activity. While ECoG offers higher temporal and spatial resolution compared to EEG, its invasive nature makes it beyond the scope of this project. Other non-invasive methods, such as Magnetoencephalography (MEG), functional Magnetic Resonance Imaging (fMRI), and Near-Infrared Spectroscopy (NIRS), were also excluded from this project due to the high cost of the required equipment.

MEG detects magnetic fields generated by neural activity, while fMRI utilizes electromagnetic fields around the head to measure blood oxygen level-dependent (BOLD) signals during brain

activity. NIRS, on the other hand, uses infrared light to penetrate the skull by a few centimeters and measures the reflected light, which varies based on the concentrations of oxyhemoglobin and deoxyhemoglobin. Further details on these methods can be found in [18].

Focusing on EEG-based BCIs, various EEG signals have been utilized to control computers, including visually evoked potentials (VEPs), slow cortical potentials (SCPs), P300 evoked potentials, and sensorimotor rhythms (SMRs). Among these, BCIs most commonly rely on VEPs and SMRs, which will be explored further below.

VEPs are electrical signals generated in the occipital lobe (located at the back of the head) in direct response to a visual stimulus. When a visual stimulus flashes at a fixed frequency, it induces a continuous oscillatory VEP known as a steady-state visually evoked potential (SSVEP). This project specifically focuses on an SSVEP-based BCI, which will be discussed in greater detail in a later section. One example of an SSVEP-based BCI is the QWERTY-style LED keyboard developed by H. Han-Jeong et al. [19]. In this system, each key on the keyboard is illuminated by an LED flashing at a unique frequency. By analyzing the user's occipital EEG using Fast Fourier Transform (FFT), the system can determine which key the user is focusing on.

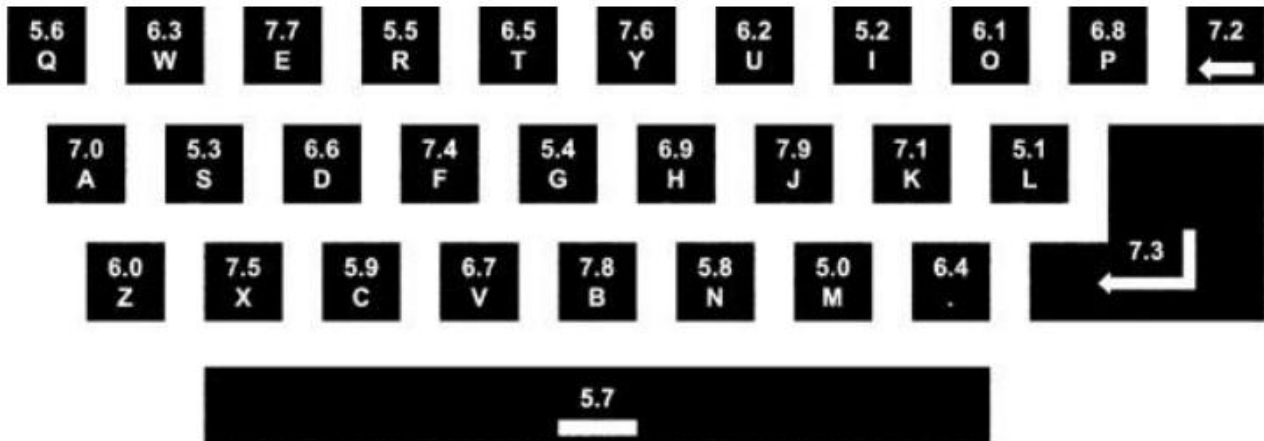


Figure 1 illustrates an example of stimulation frequency arrangements, showing 30 frequencies ranging from 5 Hz to 7.9 Hz, spaced at 0.1 Hz intervals, based on the work of H. Han-Jeong et al. [19].

Sensorimotor rhythms (SMRs), specifically mu rhythms (7-13 Hz) and beta rhythms (13-30 Hz), are oscillations that occur in the sensorimotor cortex within the motor strip (refer to Figure 8 for the motor strip's location). These rhythms are associated with motor tasks or the planning of movement. An increase in SMR activity typically indicates that a person is relaxed and not moving, while a decrease in SMR activity suggests that the person is either moving or planning to move [18]. SMR-based BCIs have been employed to control objects within 1-D, 2-D, and 3-D virtual environments, such as a virtual drone [10]. In these BCIs, two sets of electrodes are generally

placed on the left and right sides of the motor strip to monitor the brain activity related to motor tasks on each side of the body. This setup enables the user to perform four distinct actions to interact with the BCI:

- Not imagining any motor task: No reduction in SMR activity.
- Imagining a motor task on the left side of the body: SMR activity decreases on the right motor strip.
- Imagining a motor task on the right side of the body: SMR activity decreases on the left motor strip.
- Imagining motor tasks on both sides of the body: SMR activity decreases on both motor strips.

This setup provides up to four distinct actions, but typically, the options are reduced to three if the absence of SMR activity reduction is interpreted as a “do nothing” state. For optimal performance, users must train themselves to execute these motor imagery tasks, which can require weeks or even months of practice [10, 18]. In contrast, SSVEP-based BCIs do not require any training, though they are limited by the number of stimuli that can be detected within the user’s field of view. This characteristic makes SSVEP-based BCIs more suitable for users without prior training, which is why this approach was selected as the focus of this project.

2.2 THEORY BEHIND THE PROPOSED DEVICE

2.2.1 Electroencephalography

An electroencephalogram (EEG) recording system is a non-invasive tool that measures the brain's electrical activity using electrodes placed on the scalp. EEG can serve various purposes, such as evaluating a person's alertness, monitoring their responses to external stimuli, and detecting or diagnosing sleep and other neurological disorders. In recent years, however, the potential of integrating EEG signals with external devices has led to the development of BCI systems that utilize these signals to control computers [20].

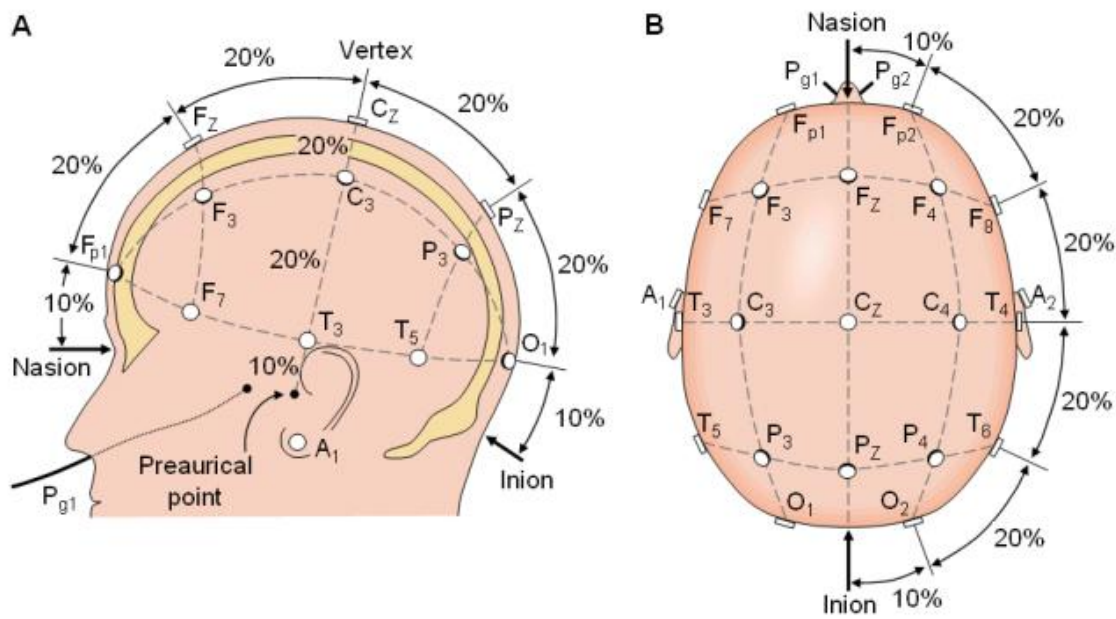


Figure 2: The 10-20 electrode placement system, shown from the (A) left side and (B) top view of the head – Image from J. Malmivuo and R. Plonsey [11].

The accuracy of the signals captured by an EEG recording system is largely influenced by the placement of the biopotential electrodes on the scalp, as well as the brain's current activity. This is because different regions of the brain are responsible for various functions. The most commonly used standard for electrode placement is the 10-20 system, as depicted in Figure 5 [11].

2.2.2 Biopotential Electrodes

Biopotential electrodes are devices used to measure the electrical potentials generated by living tissues, particularly in cells that can be activated, such as neurons or muscle cells. In EEG systems, each electrode plays a crucial role in capturing these electrical signals.

Each channel utilizes a pair of biopotential electrodes to measure the time-varying difference in electrical potential between two points on the scalp, known as a bipolar configuration, or between a single point on the scalp and a reference voltage, such as the ear, in what is called a unipolar configuration [11].

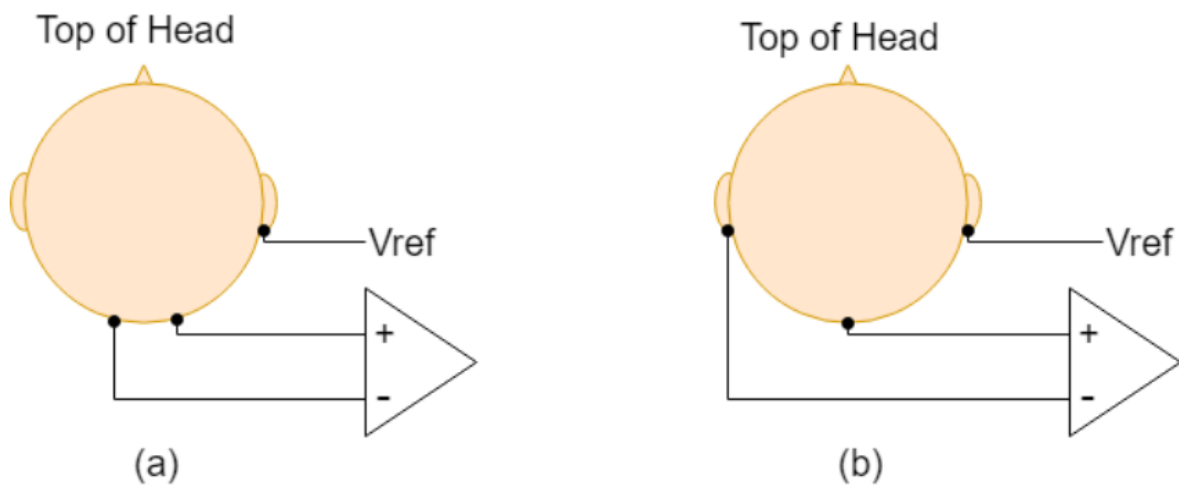


Figure 3: (a) Bipolar electrode placement (O2-O1). (b) Unipolar electrode placement (Oz-left ear)

Biopotential electrodes can be categorized into two main types: wet and dry. Wet EEG electrodes are typically cup-shaped and are filled with a conductive gel to ensure a good connection with the scalp through the hair. In contrast, dry electrodes do not require any gel; instead, they have small protrusions or teeth that penetrate through the hair to establish contact with the scalp.



Figure 4 (a) Wet EEG cup electrodes - Images from Kandel Medical [21]. (b) Dry EEG electrodes - Image from Guger Technologies [22]

Wet electrodes can become uncomfortable when worn for extended periods because the conductive gel tends to dry out, which can degrade signal quality and necessitate scrubbing the skin. This process can make the skin more sensitive, leading to discomfort for the user. On the other hand, dry electrodes are generally more comfortable and require less maintenance, but they are more prone to motion artifacts and increased electrode-skin impedance [23]. The materials used for electrodes can vary, with common types including silver/silver chloride, gold, silver, stainless steel, and tin. Reusable EEG electrodes can cost \$10 or more per lead [24], which is why this project opted for low-cost, homemade electrodes.

Electrodes can also be classified as either active or passive. Active electrodes incorporate a buffer amplifier within or near the electrode, which helps to mitigate the effects of high or variable electrode-skin impedance and reduces the impact of motion artifacts and cable movement [25]. In contrast, passive electrodes lack this buffer amplifier and are simply connected to the bio-amplifier through a long wire.

2.2.3 Steady-State Visually Evoked Potentials

As previously mentioned, different regions of the brain are responsible for various functions, so electrodes must be strategically placed to detect specific neural activities. A diagram illustrating the different brain regions is shown in Figure 8. The area of focus for this project is the occipital lobe, highlighted in pink, as the proposed BCI system relies on signals originating from this region.

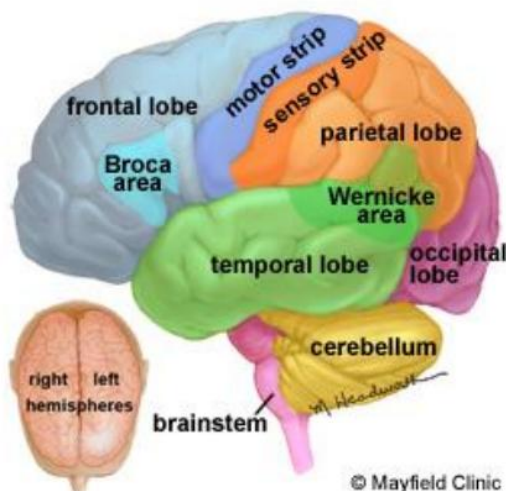


Figure 5: Figure 8 Different areas of the brain – Image from the Mayfield Clinic[1].

The occipital lobe is primarily responsible for processing visual information [26]. An electrical response in this area can be triggered by a light flashing at a constant frequency within the person's field of view [27]. The fundamental frequency of this flashing light, along with its harmonics, will appear in the EEG's frequency spectrum in this region. This type of electrical response to the flashing light is known as a steady-state visually evoked potential (SSVEP) [27].

Two examples of stimuli that have been shown to generate SSVEPs include flashing LEDs and a periodically reversing checkerboard pattern on a computer screen [18]. When using a reversing

checkerboard stimulus, the observed SSVEP frequency corresponds to the frequency at which the pattern reverses [27].

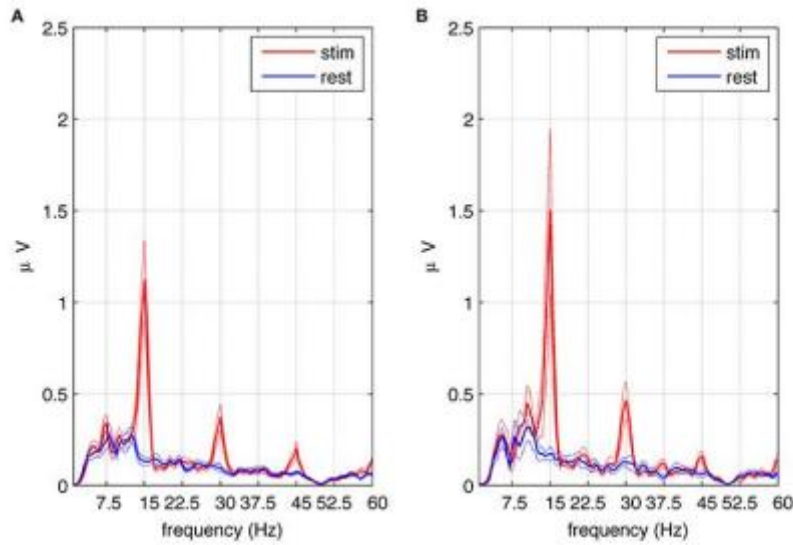


Figure 6: (Blue) Frequency spectrum of EEG without stimulus. (Red) Frequency spectrum of EEG with 15Hz stimulus showing 2nd and 3rd harmonics – Image From L. Maciej et al. [28].

To prevent distortion, the frequency of a periodic flashing stimulus displayed on a computer screen must be a divisor of the screen's refresh rate. This requirement limits the number of stimuli that can be used, and consequently, the number of options available in an interactive computer-based BCI. The presence of harmonics in the EEG's frequency spectrum can cause interference when stimuli share a fundamental frequency with the harmonics of another stimulus. For example, on a 60 Hz screen, the possible displayable frequencies include 60, 30, 20, 15, 12, 10, 6, 5, 3, 2, and 1 Hz. In this scenario, it is not feasible to have five distinct flashing stimuli that do not interfere with each other. While it is possible to overcome this issue, doing so adds complexity to the BCI system.

In contrast to stimuli displayed on a computer screen, an LED stimulus is not constrained by the screen's refresh rate and can be delivered at any frequency within the SSVEP range. SSVEPs offer a strong foundation for a BCI because they require no user training, have been shown to achieve high communication rates (exceeding 60 bits per minute), and enable a larger number of choices compared to other EEG signals using just one channel [18]. Research by Kelly et al. [28] revealed that when a subject is presented with two stimuli, they can enhance the response amplitude to one of the stimuli without shifting their gaze, simply by focusing their attention on it. This suggests that SSVEP-based BCIs have the potential to be used by individuals who are unable to move their eyes or head.

2.2.4 EEG Frequency Bands

SSVEPs are a type of event-related potential (ERP), which are electrical responses in the brain triggered by external stimuli. NonERP-related brain activity can be categorized into various frequency bands, each representing different aspects of the user's current mental state. The frequency bands into which spontaneous EEG activity is typically divided are summarized in Figure 10 [2].






Rhythm	Signal appearance	Main behavioral trait
Gamma 30-100 Hz		Represents binding of different populations of neurons for the purpose of carrying out a certain
Beta 13-30 Hz		Usual waking rhythm associated with active thinking and active
Alpha 8-13 Hz		It is usually found over the occipital regions. Indicates relaxed awareness without attention or
Theta 4-8 Hz		Theta waves appear as consciousness slips towards drowsiness. Theta increases have
Delta 1-4 Hz		Primarily associated with deep (slow) wave sleep.

Figure 7: EEG frequency bands and their corresponding mental states – Image from M.G.N. Garcia et al. [2]

Alpha waves are of particular interest in this report because their magnitude significantly increases when the eyes are closed. This characteristic can be used to quickly verify if an EEG measurement circuit is functioning correctly and if the electrodes are properly connected [29]. While alpha waves can be detected throughout the brain, they are especially prominent in the occipital lobe when the eyes are closed [18]. In the frontal lobe, alpha waves have been used to assess a user's attention, as these frequencies tend to diminish when the user is actively focusing on a task [18]. However, due to their binary nature, alpha activity is not ideal for use in complex, interactive BCIs.

2.2.5 Noise and Interference During Measurement

Accurately measuring a user's EEG can be challenging due to several factors, including ensuring a good connection between the electrode and the scalp, electrode movement, interference from mains power lines, and interference from muscle activity or other unrelated brain activity. These

issues will be discussed in this section. One critical factor is electrode-skin impedance, which refers to the varying resistance between the electrode and the skin. If this impedance is too high, it can distort and weaken the already small EEG signals. Several factors can influence impedance, such as the amount of dead skin and sweat between the electrode and the scalp, electrode movement, the type of electrode used, and the type of conductive gel applied (if any). Since EEG measurement requires at least two electrodes, managing impedance is crucial to obtaining accurate readings.

The difference in impedance between electrodes can decrease the common mode rejection ratio (CMRR) of the instrumentation amplifier (in-amp), leading to the unwanted amplification of signals common to both electrodes [30]. To reduce impedance, it is helpful to abrade the skin to remove dead skin and oils and to follow proper electrode mounting procedures. Motion artifacts are another source of interference, caused by the movement of the electrodes or wires. The magnitude of this electrical interference can be significantly higher than the EEG signal itself, which is typically less than $100\mu\text{V}$ [29], whereas electrical signals from muscle movement can reach tens of millivolts, potentially obscuring the EEG signals of interest [31]. Interference at 50 Hz (or 60 Hz) is commonly present in EEG recordings due to electromagnetic interference (EMI) from nearby electrical power lines. This interference can be much stronger than the EEG signal. Many biopotential amplifiers mitigate this interference using a driven right leg (DRL) circuit or filters, whether analog or digital. The DRL circuit actively cancels the common mode signal detected in the circuit; this will be discussed in more detail in a later section. According to Bulent et al. [32], a CMRR greater than 80 dB is essential for accurate bio signal acquisition. Electrode half-cell potentials, which result from the electrode material, temperature, and any conductive gel used, manifest as a slowly varying DC voltage on the electrode. These potentials can reach hundreds of millivolts [33], which is orders of magnitude larger than the EEG signal. If these half-cell potentials are amplified, they could potentially saturate the output of the amplifiers.

2.2.6 EEG Measurement Circuit

Most bio-amplifier circuits can be divided into four main components: the protection circuit, in-amp, gain stage(s), and mains interference rejection. This section will provide an overview of conventional designs and their functions. The protection circuit is designed to limit the current to and from the user in case of a fault. The simplest protection circuit involves placing a resistor in series with the electrode as it enters the in-amp. This resistor limits the current but does not protect

the amplifier from voltages beyond its specified range. Voltage clamping can be employed to protect the amplifier from over voltages using diodes. Two diodes can be connected to ground from each signal input, one in reverse bias and one in forward bias. These diodes will clamp the signal if the threshold voltage is exceeded, while acting as open circuits under normal conditions

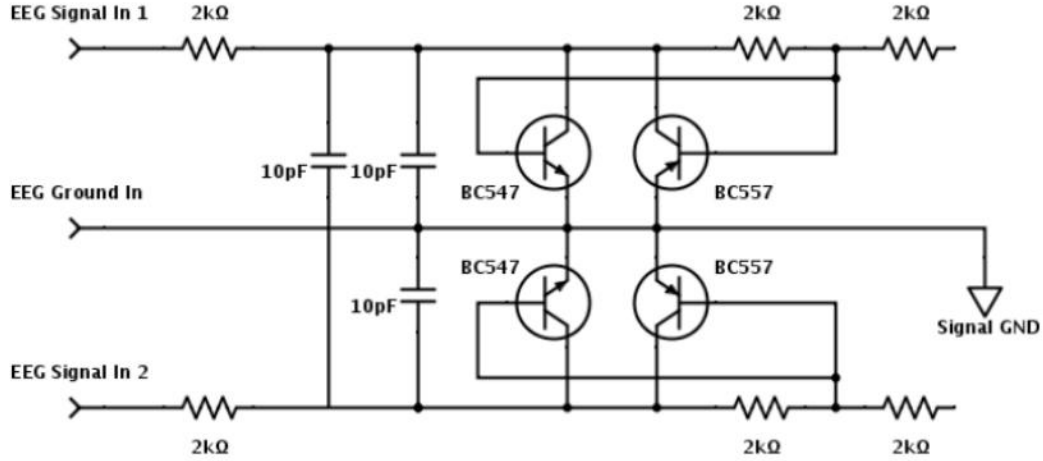


Figure 8: Example protection circuit – Image from B. Fong et al [34]

The circuit depicted in Figure 11 uses transistors instead of diodes, but they fulfill the same purpose. It is also common [29, 34, 35] to include a high cut-off, low-pass filter at the input of the protection circuit to filter out radio frequency interference (RFI) that the circuit may pick up. In the circuit above, there is a low-pass, common-mode filter on each signal line and a low-pass, differential filter shared by both lines. If the cut-off frequency of the differential filter is set to be at least an order of magnitude lower [36] than the common-mode filters, it will help compensate for mismatches between the two common-mode filters, thereby preserving the CMRR.

The output from the protection circuit is then fed into the in-amp, which amplifies the difference between the two signal lines. As mentioned earlier, a CMRR of 80 dB or higher is considered ideal for achieving a good signal-to-noise ratio when measuring biopotentials. Therefore, the components of the protection circuit should have the same values and low tolerances on each signal line. The in-amp itself should also possess a high CMRR. The gain of the amplifier should be chosen to bring the signal to a reasonable level so that the main gain stage can effectively amplify it. Typically, in-amp gains range from 5 to 20 [29, 34, 37] to prevent DC offsets caused by half-cell potentials from saturating the amplifier.

The gain stages provide additional amplification, often thousands of times in the case of an EEG

signal, to elevate the signal amplitude to a level suitable for input to an ADC. Multiple op-amp-based gain stages are commonly used to minimize the impact of input offset voltages, noise introduced by the amplifier, and reduction in amplifier bandwidth. Using a single amplifier with a large gain can limit the circuit's ability to measure the EEG effectively due to these factors. There are amplifiers available that are designed to have low input offsets and low noise relative to gain. However, using multiple stages may increase the circuit's cost and footprint. The gain stage usually incorporates highpass filtering to eliminate half-cell potentials and input offset voltages, as well as an anti-alias filter at the output.

Mains interference rejection is typically achieved in one of two ways: through the use of filters, such as notch or low-pass filters, or by employing a driven right leg circuit. Filters can effectively remove mains interference if 50 Hz/60 Hz is outside the frequency band of interest. However, if the frequency is within the band and a notch filter is used, EEG signals containing 50 Hz/60 Hz will be significantly distorted. Additionally, when using a notch filter,

The stop band of the notch filter will need to be adjusted based on the country's mains frequency where the device is being used. The driven right leg (DRL) circuit, on the other hand, is designed not to interfere with the EEG signal itself but to cancel out common mode voltages, which are primarily due to mains interference but may also include interference from other sources. A simplified diagram of a driven right leg circuit connected to a person is shown in Figure 09.

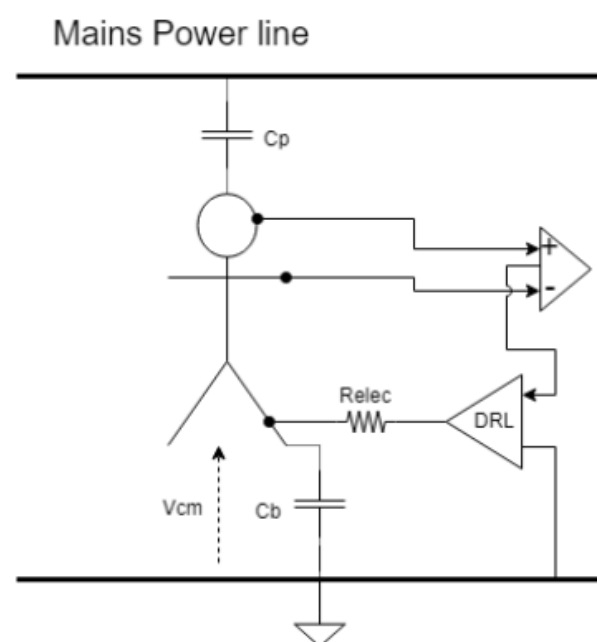


Figure 9: Biomeasurement circuit utilising a driven right leg circuit

In the diagram, the exact placement of the electrodes is not critical. Mains interference is coupled to the body through stray capacitance (C_p), and C_b represents the capacitance between the body and ground. The time-varying voltage between the body and ground is known as the common mode voltage (V_{cm}). Reducing the impedance between the body and ground will decrease the magnitude of V_{cm} , which is achieved through the DRL circuit. The simplest form of a DRL circuit is an inverting amplifier that measures the common mode voltage at the input of the in-amp, inverts and amplifies it, and then drives the DRL electrode to the resulting voltage. This process effectively creates a parallel path through the resistance "Relec" to ground when the DRL is referenced to ground. The higher the gain of the DRL, the lower the effective impedance of Relec, leading to a reduction in V_{cm} . However, if the gain is too high, it can cause instability in the closed-loop system [38]. As mentioned earlier, the DRL can also cancel out other common mode voltages on the body. Any common mode voltages detected by the in-amp will be fed into the DRL and should be neutralized, providing an advantage over relying solely on filters.

2.2.7 Feature Extraction and Probability Distributions

Feature extraction methods in biological signals range from simple techniques like thresholding [32], where the current value is compared to a threshold to determine the presence or absence of activity, to more sophisticated approaches, such as statistically based methods that estimate the probability of a signal belonging to one of several classes [39]. Before describing the naïve Bayes classifier method, it's important to first understand the fundamentals of fitting a probability density function (PDF) to data.

The probability density function (PDF) of a continuous random variable is a function that describes the likelihood of observing a particular value based on a given model of a process. Various functions can be used to model PDFs, and selecting the most appropriate one for the data is crucial for accurately representing the probability. This is typically achieved by recording a large dataset and creating a histogram. The histogram provides a discrete probability, while the PDF offers an estimated continuous probability for each value. The more observations included in the histogram, the more accurate the representation of the probability, leading to a more precise PDF. Saji et al. [40] discovered that the amplitude of EEG signals recorded from preterm infants could be effectively modeled using a log-normal distribution, a specific type of probability distribution function. The location, scale, and shape parameters of this distribution were used to estimate the infants' brain development. Figure 10 illustrates the fitting of different PDFs to the datasets from Saji et al.

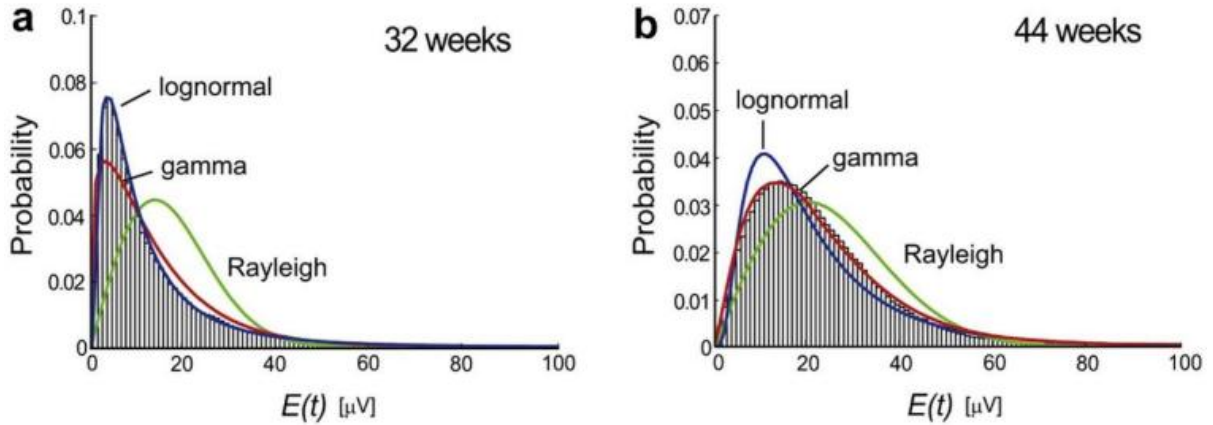


Figure 10: : Two representative histograms of the envelope and probability distributions (blue line: log-normal distribution; red: gamma distribution; green: Rayleigh distribution) for preterm EEGs. (a) An example of a probability distribution well-fitted by a log-normal distribution, with data obtained from an infant at a postconceptional age of 32 weeks. (b) An example of a probability distribution well-fitted by a gamma distribution, with data obtained from an infant at a postconceptional age of 44 weeks – Image from R. Saji et al. [40].

A widely used method for determining the parameters that best describe a PDF is the maximum likelihood estimate (MLE). This technique maximizes the likelihood function by identifying the PDF parameters that most accurately fit the observed data [41]. The location parameter defines the center of the distribution, the scale parameter determines its spread, and the shape parameter reflects the skewness of the PDF. For instance, the PDFs illustrated in Figure 13 are skewed to the left. After determining the MLE parameters for different PDFs, these can be compared using the negative log-likelihood function. A smaller negative log-likelihood value indicates a better fit of the MLE to the data [42].

In classification tasks where each observation must be assigned to one of several discrete classes, a PDF may be provided or estimated for each class. In such scenarios, a naive Bayes classifier is an effective method for predicting the likelihood that an observation belongs to each class, thereby helping to identify the most probable class. The equation for the naive Bayes classifier is presented below.

$$p(C_k|x) = \frac{p(x|C_k) * p(C_k)}{p(x)} = \frac{p(x|C_k) * p(C_k)}{p(x|C_n) * p(C_n) + \dots p(x|C_{N-1}) * p(C_{N-1})} \quad (1)$$

C_k	Class k
x	new observation
$p(C_k x)$	probability of C_k given x (posterior)
$p(x C_k)$	probability of x given C_k (likelihood)
$p(C_k)$	probability of C_k (prior)
$p(x)$	probability of x (sum of the probability of x given each class multiplied by the prior probability of that class)
N	number of classes
n	class n , $0 \leq n < N$

To illustrate a naïve Bayes classifier, we can use the PDFs provided by Saji et al. as an example, though this is not the statistical method recommended by the author later in the report. Consider the two PDFs in Figure 13 as representing two distinct classes. Now, suppose a new EEG observation of 30 μ V is recorded, and the infant's age is either 32 weeks or 44 weeks postconceptional age (PCA). Since these are the only two possibilities, the sum of the probabilities for these two classes (32 weeks and 44 weeks) must equal one. Imagine that 10 infants were previously tested, with 6 of them being 32 weeks PCA. This would result in:

$$p(C_{32weeks}) = \frac{6}{10} = 0.6 \quad p(C_{44weeks}) = 1 - 0.6 = 0.4 \quad (2)$$

This is the prior probability created from previous data. Now using the 30 μ V reading, the likelihood of this reading in each class can be measured from the PDFs (using the log-normal PDF for the 32 weeks data and the gamma PDF for the 44 weeks data).

$$p(30 \mu V | C_{32weeks}) \cong 0.005 \quad p(30 \mu V | C_{44weeks}) \cong 0.015 \quad (3)$$

The probability that the observed value is from a 32 week PCA or a 44 week PCA infant is shown below:

$$p(C_{32weeks} | 30\mu V) = \frac{p(30 \mu V | C_{32weeks}) * p(C_{32weeks})}{p(30 \mu V | C_{32weeks}) * p(C_{32weeks}) + p(30 \mu V | C_{44weeks}) * p(C_{44weeks})} \quad (4)$$

$$= \frac{0.005 * 0.6}{0.005 * 0.6 + 0.015 * 0.4} = 0.3333$$

$$p(C_{44weeks} | 30\mu V) = 1 - 0.333 = 0.667 \quad (5)$$

It is more likely that this observation comes from a 44-week PCA infant than a 32-week one. This example illustrates how a naïve Bayes classifier operates with two classes and a single observation, but the classifier can also be applied to multiple classes and observations. When multiple observations are used in a single probability estimation, each observation is "naively" assumed to be completely independent of the others. For a more detailed explanation of the theory behind naïve Bayes classifiers, refer to Murphy [43].

3. METHODOLOGY

The proposed methodology involves acquiring a single-channel SSVEP-based EEG signal using three electrodes. The captured signal will then be amplified and processed to remove noise and artifacts. Following this, feature extraction will be performed to identify relevant signal characteristics. The extracted features will be classified, and finally, a BCI software system will be developed to utilize the classified signals for home automation control.

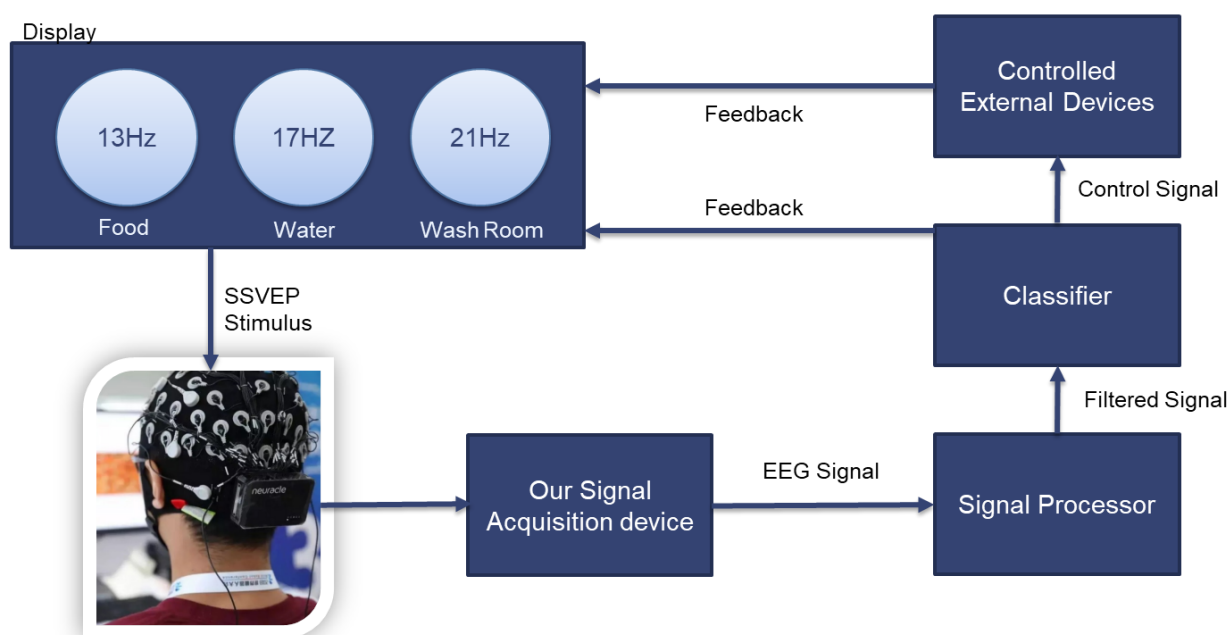


Figure 11: Overview of the System Functionality for an EEG-Based Brain-Computer Interface (BCI) System

The proposed methodology outlines the steps required for the design and implementation of an EEG-Based Brain-Computer Interface (BCI) system for home automation control.

1. Signal Acquisition:

The process begins with the acquisition of EEG signals using three electrodes. The signals are captured from the user's scalp, specifically targeting the visual cortex where SSVEP responses are most prominent.

2. Signal Processing:

Once captured, the EEG signals are amplified and processed to remove noise and artifacts. This step ensures that the signals are clean and suitable for further analysis.

3. Feature Extraction:

After preprocessing, relevant features from the EEG signals are extracted. These features represent the characteristics of the SSVEP responses that are critical for distinguishing different mental states.

4. Classifier Design:

A classification algorithm is then designed to categorize the extracted features. This step involves training a classifier to accurately differentiate between the various SSVEP-based signals.

5. User Interface and Software Design:

A user-friendly interface is developed to interact with the classified signals. The software system interprets the classified outputs and allows users to control home automation devices via the BCI system.

6. Integration with External Devices:

The classified signals are integrated with external home automation devices, enabling the user to control them through the BCI interface. This step involves communication protocols and hardware interfaces to ensure seamless operation.

7. Testing and Evaluation:

Finally, the system undergoes comprehensive testing and evaluation to assess its performance, accuracy, and reliability. The system is fine-tuned based on test results to achieve optimal functionality.

3.1 SIGNAL ACQUISITION

3.1.1 Circuit Design

The EEG signal typically ranges between 1-100 μV , requiring significant voltage amplification before it can be sampled by the microcontroller. However, interference from both the electrodes and the circuit itself can introduce noise that might exceed the amplitude of the EEG signal. This interference needs to be filtered out or otherwise mitigated to ensure that the EEG signal can be amplified without causing saturation of the amplifier. This was the primary objective in the design of the EEG measurement circuit. In addition, the circuit's complexity and cost were considered during the selection of components.

The circuit design includes various stages, including a protection circuit, amplification stages,

filters, and a driven right leg (DRL) circuit.

The main components of the EEG measurement circuit are shown in the block diagram in Figure 12. The electrodes are placed according to the 10-20 system, with connections to the Oz, left mastoid, and right mastoid regions of the head. This configuration helps in capturing the EEG signals effectively for processing and analysis.

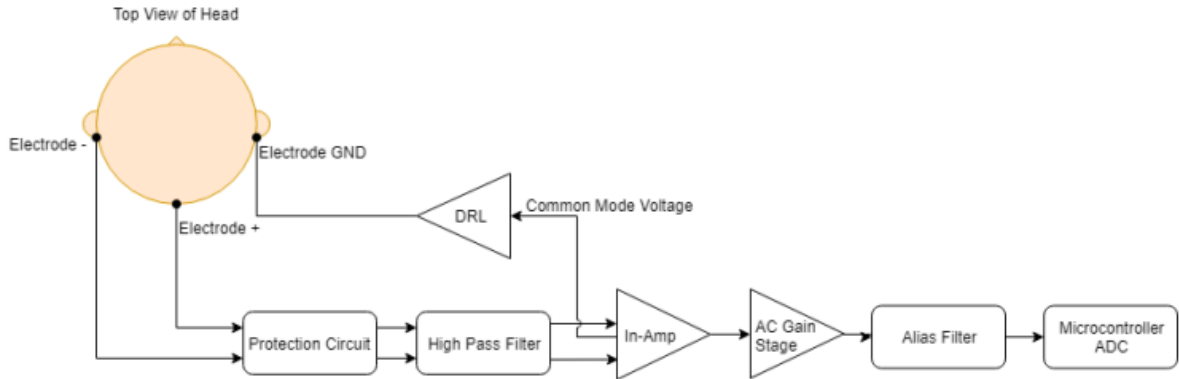


Figure 12: Block diagram of EEG measurement circuit connected to the user

The EEG signal is measured between Oz and the left mastoid (unipolar), with the right mastoid connected to the output of the DRL. The ESP32 microcontroller was chosen for its compact size, high processing power, integrated Wi-Fi and Bluetooth capabilities, and its compatibility with external ADCs. To enhance resolution, the ADS1115 ADC was integrated, increasing the bit resolution to 16 bits, providing more precise signal measurements. Compared to an Arduino Nano, which has a similar form factor, the ESP32 combined with the ADS1115 offers significantly better performance. Additionally, the author aimed to utilize the advanced features of the ESP32 and ADS1115 for improved accuracy and functionality. Figure 16 shows the completed circuit on a breadboard, excluding external connections such as electrode wires, battery, or serial output.

The total cost of the circuit was approximately \$33.09, with the cost per electrode being \$0.77. Many components were purchased in sets, and the unit cost was estimated by dividing the total cost by the number of units in the set. This cost applies to a single-channel EEG measurement circuit. For additional channels, the ESP32 microcontroller, optoisolation circuit, and DRL can be reused, reducing the cost to \$5.49 per additional channel. The ESP32 supports a maximum of nine channels due to its available ADC inputs. However, the sample rate and processing speed of the ESP32, in combination with the ADS1115, may impose limitations on the practical number of channels.

The theoretical input voltage specifications for the circuit are summarized in Table 1. The maximum peak-to-peak amplitude at the ADC pin is 3 V, or a peak amplitude of 1.5 V, as voltages exceeding this

will cause negative peak clipping. With the integration of the ADS1115, the resolution is increased to 16 bits, improving the accuracy of measurements beyond the default 3.3 V, 12-bit resolution of the ESP32's internal ADC.

Table 1: Table of theoretical input voltage specifications for the circuit

Values	At Minimum Gain	At Maximum Gain
Gain	51	25500
Input Max Peak-Peak	58.8 mV	117.6 μ V
Input Resolution	15.8 μ V	31.6 nV
Max Input DC	± 500 mV	± 500 mV

3.1.2 Protection Circuit

The EEG electrodes connect to the protection circuit, which serves to safeguard both the user and the circuit from high voltages and currents. The design of the protection circuit, shown in Figure 13, is a common approach used in EEG measurement systems, with component values adapted from previous designs [35].

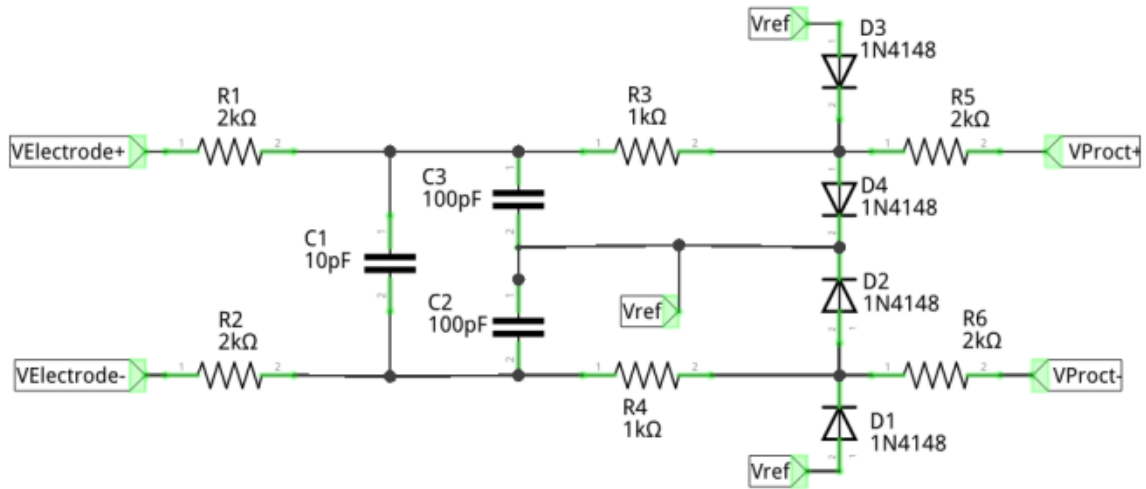


Figure 13: Circuit diagram of the protection circuit. VElectrode is the input from the positive and negative electrode. VProct is the positive and negative output of the protection circuit

The input signals from the electrodes first pass through both differential and common-mode low-pass filters. The common-mode filters, consisting of R1 and C3, and R2 and C2, are designed to filter out electromagnetic interference (EMI) on each signal line, including potential radio frequency interference. Meanwhile, the differential filter, formed by R1, R2, and C1, acts as a second-order low-pass filter on both signal lines. The transfer functions of these filters are outlined

below, ensuring effective noise reduction and signal integrity.

$$\frac{V_{filtDiff}(s)}{V_{inDiff}(s)} = \frac{1}{(R_1 + R_2)C_1s + 1} = \frac{1}{40 * 10^{-12}s + 1} \quad (6)$$

$$\frac{V_{filtCm}(s)}{V_{in}(s)} = \frac{1}{R_1C_2s + 1} = \frac{1}{200 * 10^{-12}s + 1} \quad (7)$$

After passing through the filters, the signal is further processed by two resistors that limit the current on each line. Following this, 1N4148 diodes are used to clamp the input voltage before it reaches the next stage, which is the instrumentation amplifier. These diodes begin conducting around 500 mV and act as open circuits for voltages below this threshold. Consequently, any voltage within ± 500 mV relative to the reference voltage (V_{ref}) passes through this stage unaffected. The EEG signals, typically in the microvolt range, along with small DC offsets of tens of millivolts caused by half-cell potentials, remain intact during this process. Figure 14 illustrates the input and output of the protection circuit when subjected to both a 140 mV and a 2 V peak-to-peak input.



Figure 14: (a) Input (yellow) and output (blue) of protection circuit from input within the normal operating range. (b) Input (yellow) and output (blue) of protection circuit from input outside the normal operating range.

In Figure 14 (a), the output is almost unaffected by the protection circuit but in Figure 14 (b) with a much larger input voltage, the diodes clamp the voltage leaving the protection circuit.

3.1.3 Instrumentation Amplifier

The output of the protection circuit is then connected to the instrumentation amplifier (in-amp), which amplifies the voltage difference between the two electrodes. To prevent the amplification

of DC voltages caused by half-cell potentials, high-pass filters are applied to the in-amp inputs. These filters have a cutoff frequency of 0.159 Hz, effectively blocking unwanted DC offsets. The resistors R3 and R4 are set to 1 M Ω to maintain the high input impedance of the in-amp, ensuring accurate signal amplification without significant signal loss.

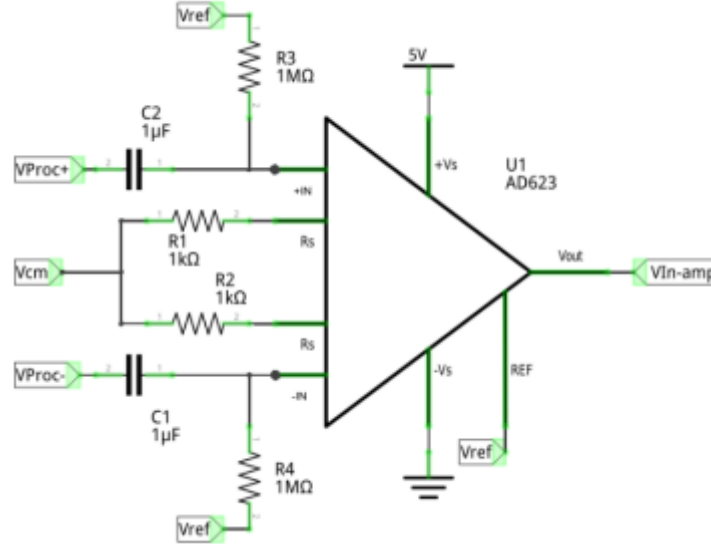


Figure 15: Circuit diagram of the instrumentation amplifier. VProc+ is the positive and negative output from the protection circuit. Vcm is the common mode voltage measured by the in-amp. Vin-amp is the output of the in-amp. Vref is the 1.5 V reference voltage

The in-amp used in this design is the Analog Devices AD623, selected for its high CMRR with a mean value of 80 dB, single-supply operation, and rail-to-rail output. After filtering out the DC components, the amplifier focuses on the AC components of the signal, providing a gain of 51, which is achieved using two 1k Ω resistors. The gain (A_{inAmp}) of the AD623 is calculated as follows:

$$A_{inAmp} = \frac{100k}{R_g} + 1 = \frac{100k}{1k + 1k} + 1 = 51 \quad (8)$$

This gain is higher than what is typically used in bio-amplifier circuits [35, 37], as most designs do not filter out the DC offset before entering the amplifier and must limit the gain to prevent

$$V_{cm} = \frac{V_{inAmp_{in+}} + V_{inAmp_{in-}}}{2} \quad (9)$$

saturation of the output. Additionally, the common-mode voltage (V_{cm}) at the in-amp inputs is measured at the midpoint between the two gain resistors and is calculated as follows:

V_{inAmp+} Input voltage at the positive input of in-amp

V_{inAmp-} Input voltage at the negative input of in-amp

V_{cm} is utilized in the driven right leg (DRL) circuit to enhance the overall common-mode rejection ratio (CMRR) of the system, as detailed in Section 3.1.5. The transfer function of the in-amp circuit, from the input of the high-pass filters to the output, is provided below.

$$\frac{V_{inAmp_{out}}(s)}{V_{inAmp_{in+}}(s) - V_{inAmp_{in-}}(s)} = A_{inAmp} * \frac{s}{s + \frac{1}{C_1 R_4}} = 51 * \frac{s}{s + 1} \quad (10)$$

A high CMRR is crucial for separating the EEG signal from interference, particularly the 50 Hz mains noise. The AD623 in-amp has a mean CMRR of 80 dB, as specified in the datasheet, which applies to the amp alone without any additional components. While the in-amp can significantly suppress 50 Hz interference on its own, the CMRR can decrease if the components in the circuit are not precisely matched.

To address this, metal-oxide film resistors with a low tolerance of 1-2% were used in the protection circuit, as opposed to carbon film resistors, which typically have a 5% tolerance. However, variations in electrode-skin impedance can also reduce the CMRR. For this reason, a driven right leg (DRL) circuit is incorporated to further enhance the overall CMRR of the system.

3.1.4 Gain Stage and Alias Filter

The output of the in-amp is connected to a gain stage using the TLC2274 quad op-amp, which provides a variable AC gain of approximately 1-501, adjusted by changing the value of R_5 (as shown in Figure 16). The TLC2274 was selected for its rail-to-rail output, low noise, and low input offset voltage. The DC gain is set to approximately 1, allowing DC signals to pass through without amplification, while AC components are amplified. The cutoff frequency of this gain stage is around 0.338 Hz.

Upon powering the circuit, C_1 needs to charge to V_{ref} , which occurs through R_5 and R_4 . To expedite this process, R_5 is initially set to a low resistance and then increased to the desired gain once the circuit has stabilized. The transfer function for this gain stage is provided below.

$$\frac{V_G(s)}{V_{inAmp_{out}}(s)} = \frac{R_5 C_1 s}{R_4 C_1 s + 1} + 1 = \frac{R_5 * 470 * 10^{-6} s}{0.47 * 10^{-6} s + 1} + 1 \quad (11)$$

V_G Output voltage from gain stage

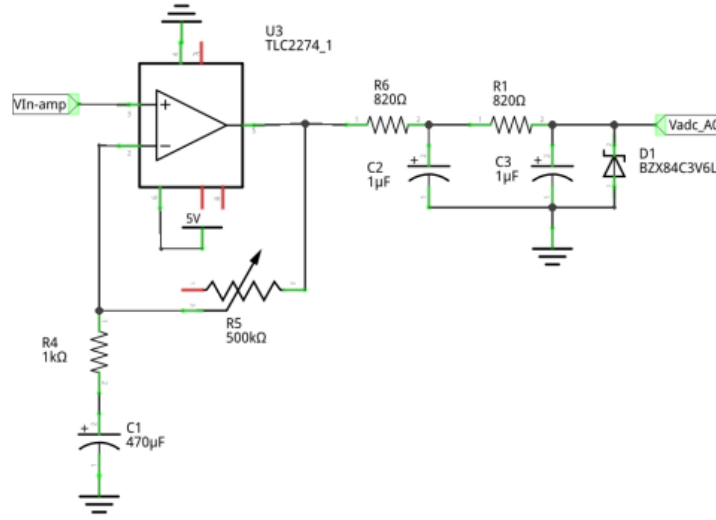


Figure 16: Circuit diagram for gain stage and alias filter. *Vin-amp* is the output of the in-amp. *Vadc_A0* is the output of the alias filter connected to analog pin A0 on the on the future selected development board (ADS1115)

The output of this gain stage is connected to a second-order passive low-pass filter to block any high frequencies from entering the ADC. This step is crucial for reducing the risk of aliasing in the digital signal. The filter has a cutoff frequency of 194 Hz, which effectively preserves the frequencies of interest in this application (5-20 Hz) while significantly attenuating frequencies above the Nyquist frequency of 500 Hz. The transfer function of this filter is provided below.

$$\frac{V_{lp}(s)}{V_G(s)} = \left(\frac{1}{R_6 C_2 s + 1} \right) \left(\frac{1}{R_1 C_3 s + 1} \right) = \left(\frac{1}{820 * 10^{-6} s + 1} \right) \left(\frac{1}{820 * 10^{-6} s + 1} \right) \quad (12)$$

V_{lp} Output voltage from low pass filters

Lastly, before reaching the ADC pin of the microcontroller, the output of the alias filter is connected to a 3.6 V Zener diode in reverse bias, which is connected to ground. Since the ADC pin is 3.3 V tolerant with a maximum rating of 4 V, the Zener diode starts conducting as the voltage approaches its breakdown point, effectively limiting the voltage to around 3.6 V.

A 3.3 V Zener diode was initially tested, but it began conducting at around 2.5 V, which caused clipping at the top of the waveform entering the ADC. Therefore, a 3.6 V Zener diode was used to accommodate a larger voltage range. At an input of 5 V, the 3.6 V Zener diode successfully clamped the output voltage at 3.27 V. This setup helps prevent non-linear distortion of the signal, which would otherwise result in an incorrect FFT of the input signal.

3.1.5 Driven right leg circuit

The DRL circuit utilizes the common-mode voltage measured by the in-amp, inverts it, amplifies it, and then drives it back into the DRL electrode. This process helps to counteract interference present on the body or within the circuit itself. The design of the DRL circuit is illustrated in Figure 22.

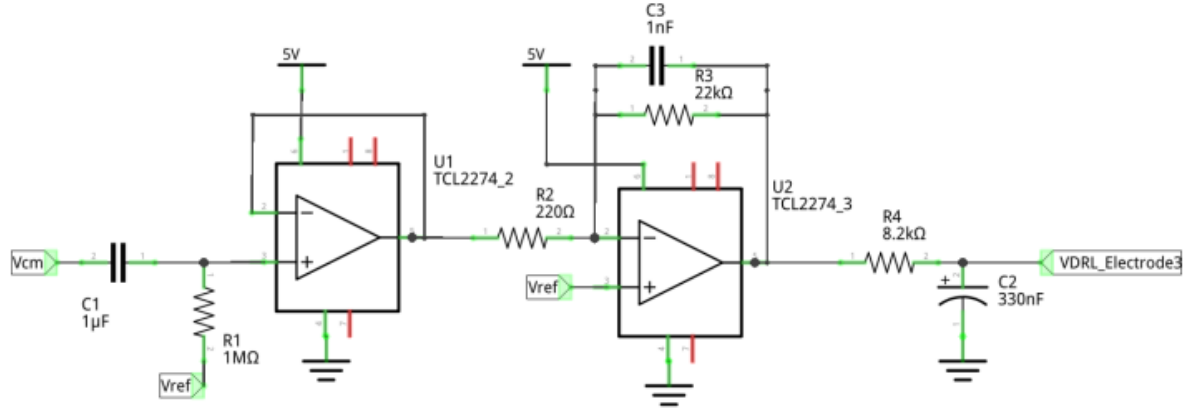


Figure 17: Circuit diagram for the driven right leg. V_{cm} is the common mode voltage measured by the in-amp. $VDRL_Electrode3$ is the output of the DRL connected to the third electrode. V_{ref} is the 1.5 V reference voltage

The common-mode voltage (V_{cm}) first passes through a high-pass filter to remove its DC component. A 600 mV offset was present due to transistors at each signal input of the in-amp, which needed to be filtered out before reaching the DRL to prevent saturation of its output. The same component values used for the in-amp high-pass filter were applied before feeding the signal into a buffer amplifier (TCL2274).

After the buffer amp, the signal goes through a low-pass, inverting op-amp (TCL2274). The gain for DRL circuits typically ranges from -10 to -100, and while a variable resistor (R_{10}) would have been ideal to adjust the gain, space limitations on the breadboard led to the use of a fixed 220Ω resistor, resulting in a gain of 100.

Due to the two cascaded high-pass filters before the DRL, the phase of the input signal to the DRL led the common-mode voltage on the body, potentially causing instability. Since the measured V_{cm} was out of phase with the actual V_{cm} , the DRL could have amplified the common-mode voltage instead of canceling it. This phase issue was corrected by adding capacitors ($C3$ and $C2$) and resistor ($R4$). After these adjustments, no instability was observed in either simulations or actual testing.

Additionally, R4 limits the amount of current that can flow into the user from the DRL. The transfer function for the DRL circuit is provided below.

$$\frac{V_{DRL}(s)}{V_{buff(s)}} = \left(-\frac{R_3}{R_2} * \frac{1}{1 + R_3 C_3 s} \right) \left(\frac{1}{R_4 C_2 s + 1} \right) = \left(-100 * \frac{1}{1 + 22 * 10^{-6} s} \right) * \left(\frac{1}{2.703 * 10^{-3} s + 1} \right) \quad (13)$$

It would be expected that the increase in CMRR from the DRL would be equal to its gain which in this case is 40 dB.

$$CMRR_{DRL} = 20 * \log_{10}(A_{DRL}) = 20 * \log_{10}(100) = 40dB \quad (14)$$

Finally, the output of the DRL is connected to the third electrode to act as the ground electrode.

3.1.6 CMRR of Circuit

The common mode rejection ratio was measured for the circuit with and without the DRL circuit to see its effect. The common mode rejection ratio is given by:

$$CMRR = 20 * \log_{10}\left(\frac{A_{diff}}{A_{cm}}\right) \quad (15)$$

A_{diff} Differential Gain

A_{cm} Common Mode Gain

The CMRR of the circuit was tested using the Bitscope Micro (a USB oscilloscope and signal generator). To allow the DRL to drive the signal up and down, the signal generator needed to be floating and not connected to the earth. The Bitscope was then set up to generate a differential signal, as illustrated in Figure 18.

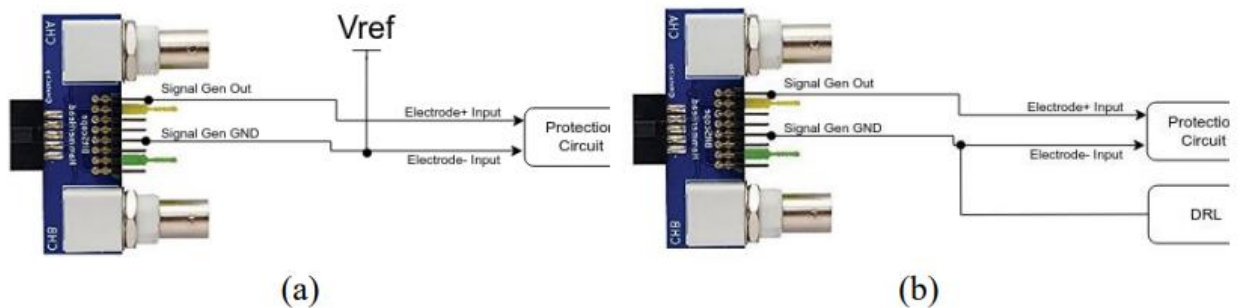


Figure 18:(a) Bitscope Micros ground connected to Vref, generating a differential signal into protection circuit. (b) Bitscope Micros ground connected to DRL, generating a differential signal – Image adapted from Amazon [45]

A 300 mV signal at 10 Hz, 50 Hz, and 100 Hz was input into the circuit, and the output (after the alias filter) was measured. To prevent the op-amps from saturating, the gain of the in-amp was reduced to 6, and the gain stage was set to 1. The Bitscope was then configured to generate a common-mode signal, as shown in Figure 19.

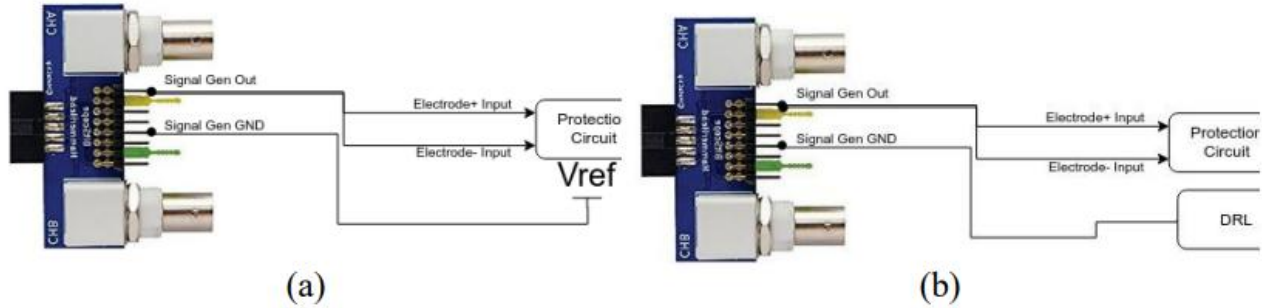


Figure 19:(a) Bitscope Micros ground connected to Vref, generating a common mode signal into protection circuit. (b) Bitscope Micros ground connected to DRL, generating a common signal into protection circuit – Image adapted from Amazon [45]

The in-amp gain was set to 6, while the gain stage was adjusted until the common-mode signal was clearly visible and measurable on the oscilloscope. The resistance of the variable resistor in the gain stage was then measured to determine the gain. The measured output was divided by this gain to ensure that both the differential signal and the common-mode signal had the same overall gain. The calculated CMRR values at each frequency, both without and with the DRL, are summarized in Table 2.

Table 2: CMRR of the circuit without the DRL and with the DRL at 10 Hz, 50 Hz and 100 Hz

Frequency (Hz)	Vref CMRR(dB)	DRL CMRR(dB)
10	53.00	78.84
50	54.92	89.99
100	55.58	86.75

From the three tests conducted, the DRL increased the CMRR by approximately 30 dB, with the highest CMRR of 35 dB achieved at 50 Hz, which is close to the expected value of 40 dB.

3.1.7 Frequency Response of the Circuit

The frequency response of the circuit's output (after the alias filter) was designed to have a passband between 5 Hz and 20 Hz, encompassing all the SSVEP stimuli. The DRL was designed with a passband from 1 Hz to 100 Hz, with optimal performance between 50 Hz and 60 Hz to counteract the main sources of interference. It is crucial that the DRL maintains a constant phase

response of -180° throughout its passband to prevent instability caused by phase lead or lag in the closed loop. The frequency response was tested using the Bitscope Micro signal generator.

For the circuit output response, the setup was connected as shown in Figure 23(b), while the DRL response was tested using the setup in Figure 24(b). The lowest frequency the Bitscope could generate was 5 Hz. During both tests, the gain of the in-amp was set to 6, and the gain stage was set to 1.

The frequency response was also simulated in LTspice using an input voltage of 136 mV for the output response and 220 mV for the DRL response. In the LTspice simulation, all components were modeled as ideal except for the in-amp (AD623) and the Zener diode (BZX84C3V6). LTspice calculates magnitude values in dB relative to 1 V, so the measured values were processed similarly for consistency.

$$A_V = 20 * \log_{10} \left(\frac{V_{out}}{1V} \right) \quad (16)$$

Figure 20 shows the frequency response of the circuit's output. The measured gain and phase graphs closely match the simulated response, except for the first data point at 5 Hz, which may indicate the presence of additional high-pass filtering not accounted for in the simulation. The gain at 5 Hz is 1.28 dB, which remains above the -3 dB point from the maximum gain of 3.17 dB, indicating it is still within the passband.

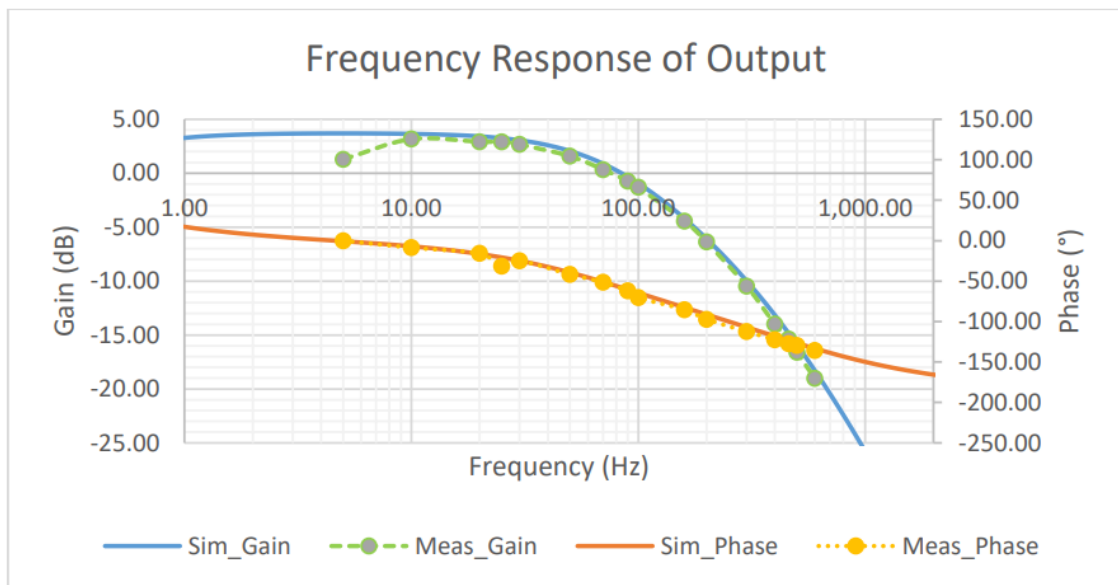


Figure 20: Figure 20: Frequency response of circuit output (simulated and measured)

The gain between 10 Hz and 20 Hz is relatively flat, averaging around 3 dB, and it sharply decreases beyond this range, reaching -16.5 dB at 500 Hz. This ensures that frequencies above the Nyquist frequency of 500 Hz are effectively suppressed. The measured passband of the circuit is approximately 3-75 Hz, as these correspond to the -3 dB points on the measured graph. The phase response was not a design consideration for SSVEP measurements, so it was not specifically optimized.

Figure 21 shows the measured and simulated frequency responses of the DRL circuit. Similar to the output response, some high-pass filtering is evident in the measured results but was not observed in the simulation. Since this additional high-pass filtering appears in both the DRL and output responses, it is likely originating from the protection circuit or the in-amp.

At the upper end of the frequency spectrum, the measured gain response rolls off a few kHz earlier than the simulated response. This discrepancy may be due to additional low-pass filtering within the closed-loop circuit that was not modeled in the simulation.

The phase response between 5 Hz and 400 Hz remains close to -180° , indicating a measured bandwidth of 395 Hz for the DRL. However, the primary frequency of concern for the DRL is 50

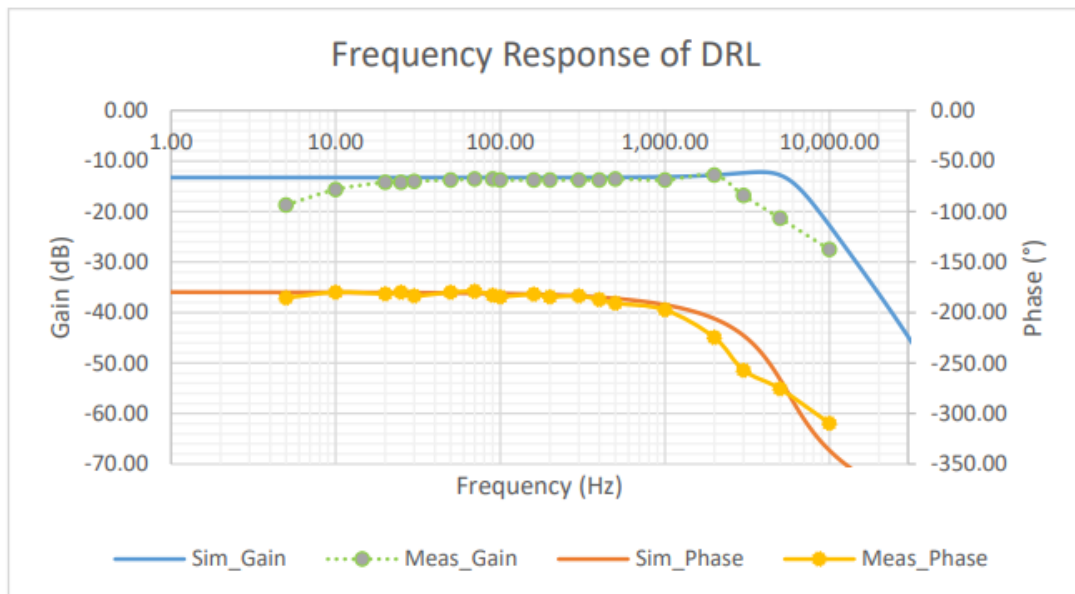


Figure 21: Frequency response of DRL (simulated and measured)

Hz, which requires compensation. As shown in the graphs, both the gain and phase at 50 Hz align well with the simulated response, confirming that the DRL operates as intended.

Overall, the circuit performs as expected. A simulated frequency response for both the output and DRL over a broader range of frequencies at full gain is provided in Appendix C - Simulated Frequency Responses.

3.1.8 Electrodes

EEG electrode cups can be prohibitively expensive for a low-cost project, often costing \$10 or more per lead. To address this, low-cost, reusable EEG electrode cups were created. This was achieved by modifying standard disposable ECG electrode pads, which are available in bulk (packs of 50) at a very affordable price. The modification involved cutting out the center of an ECG electrode pad and attaching a rubber shower hose washer to it using adhesive. This approach provided a practical and economical solution for creating reusable electrodes.



*Figure 30 (a) Top: Custom-made EEG cup electrode attached to a button snap.
Bottom: Button snap detail.*

The electrode has a diameter of 10 mm, and shower hose washers with an inner diameter of 10 mm were super-glued onto it to create a reservoir for conductive gel. The washers have a depth of 2 mm, providing an inner volume of 157 mm³, which is comparable to large dome EEG cups with a volume of 137 mm³ [46]. The electrodes are connected using a standard 13 mm metal button snap, resulting in a cost of less than €1 per electrode. These electrodes are classified as passive wet electrodes.

All electrodes used were non-shielded, multi-strand wires. To minimize electromagnetic interference (EMI), the measurement electrode wires were tightly twisted together along their length.

3.2 SOFTWARE

This section focuses on the design and non-user testing of the microcontroller software and the BCI software.

3.2.1 Microcontroller

The ESP32 was programmed using the Arduino IDE, a lightweight and user-friendly integrated development environment (IDE). The Arduino framework simplifies development by offering high-level APIs, making the code easily portable and suitable for open-source projects. This aligns with the project's goal of ensuring code reusability and accessibility. For this project, the ESP32's built-in ADC and serial communication features were utilized. The initialization code was

manually written to configure the required peripherals, including one ADC pin for signal acquisition, a UART for serial communication, and a timer for consistent sampling. The ESP32's internal clock settings were adjusted to achieve accurate sampling rates and communication speeds.

At startup, the ESP32 establishes a handshake with the connected PC to ensure proper communication and avoid byte misalignments. The ADC samples data at 1 kHz, which is sent to the PC in chunks of 256 samples via the UART interface. The UART communication is configured to run at a baud rate of 57,600. To ensure efficient data handling and avoid blocking operations, the code utilizes the ESP32's FreeRTOS-based multitasking capabilities and non-blocking functions for ADC sampling and UART transmission. A flow diagram of the ESP32 code can be found in Appendix D - ESP32 Code Flow Diagram, with the complete code included in the appendix.

3.2.2 PC

The PC software is written in Python 3.13.1 and is divided into two primary scripts: the real-time plotting window and the user interface, both of which are managed by a “master” script. To ensure predictable performance, both scripts operate on the main thread. The “master” script launches them as separate processes and connects them using a pipe, enabling seamless data sharing between the two.

3.2.2.1 Plotting Real-Time Data

The first script, named `eegScope.py`, utilizes the PyQtGraph library to generate real-time EEG and FFT plots. Upon startup, it initializes a window containing the plots, sets a timer to update them, and creates a thread to handle serial port communication. The serial thread waits for the microcontroller to complete a handshake before proceeding. Data from the serial buffer is then plotted in real time as it is received.

When one second of new data is collected, it is sent to the interface script via a pipe, and an FFT is plotted using a Hamming window. The plotted data and the sampling rate of the ESP32 were validated by feeding a sinusoidal signal of a known frequency from a signal generator into the ADC pin and confirming that the FFT peaks matched the input frequency. For example, a 20 Hz sine wave input is shown in Figure 31. The flow diagram of eegScope.py is available in Appendix E – BCI Code Flow Diagrams, and the full code is provided in Appendix F – BCI Code and on the CD included at the back of the appendix.

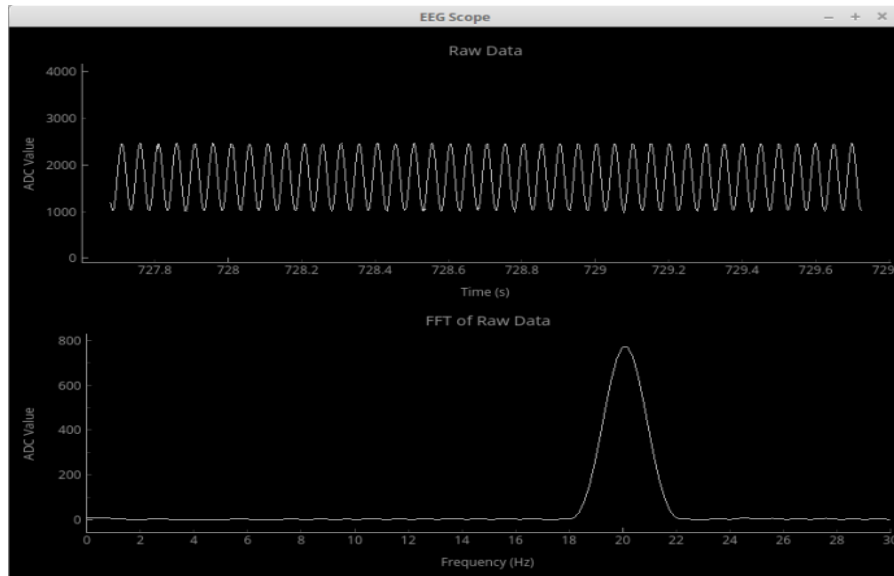


Figure 31: Real-time plot of a 20 Hz input signal.

3.2.2.3 User Interface

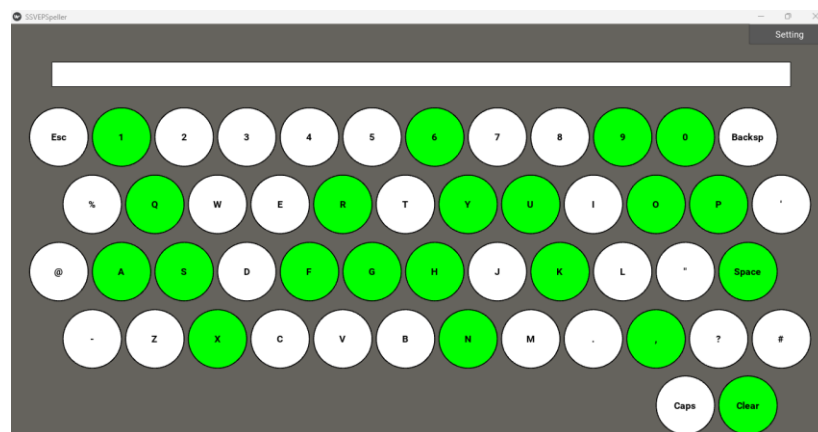


Figure 32: Settings Interface for Configuring DFBC Frequencies and Key Mappings.

The user interface was developed using Kivy (Python framework) and features a virtual keyboard with 48 keys, as shown in Figure 32. Each key is mapped to specific flickering frequencies (10 Hz, 12 Hz, 14 Hz, and 16 Hz) using a dual-frequency biased coding (DFBC) scheme, as illustrated in Figure 34. This coding scheme ensures unique frequency combinations for each key, enabling

precise and efficient selection in an SSVEP-based system. Users can interact with the keyboard simply by looking at the desired key, allowing for hands-free text input.

The virtual keyboard in Figure 32 supports real-time interaction, where the user selects keys by focusing their gaze on the flickering frequency corresponding to the intended key. This interaction is facilitated by the SSVEP detection algorithm, which interprets the EEG signal to identify the focused frequency, thereby selecting the key.

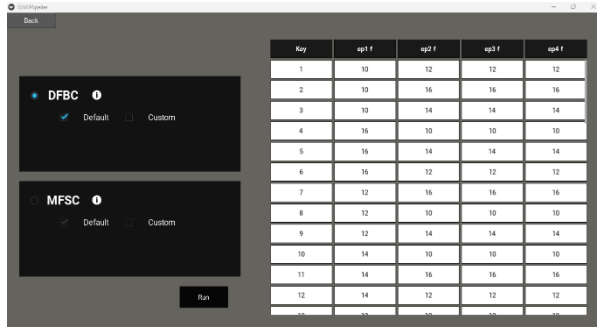


Figure 33: DFBC Configuration and Key Mapping Interface.

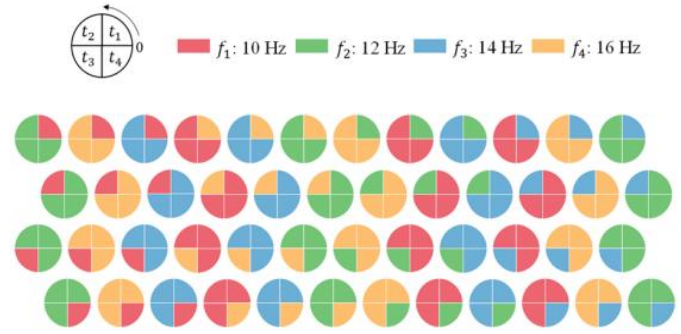


Figure 34: DFBC, using four epochs and four frequencies to code the SSVEP stimuli.

The second interface window, displayed in Figure 33, includes configuration options for the DFBC scheme. Users can toggle between default and custom settings, view the frequency assignments for each key, and adjust parameters for testing and optimization. The frequency combinations (ep1 f, ep2 f, etc.) for each key are shown in a detailed table for clarity.

Figure 34 illustrates the DFBC coding scheme, demonstrating the flickering frequency assignments for the keyboard. This innovative approach enhances the accuracy and robustness of the system, making the interface user-friendly and efficient for EEG-based applications.

3.2.2.3 Recording Baseline and Feature Extraction

At startup, the interface instructs the user to focus on the center of the screen while a baseline is recorded for 30 seconds. During this period, an FFT is calculated for each second, and the magnitudes at the stimulus frequencies are stored. After the 30 seconds, all collected values are used to create a probability density function (PDF). The most appropriate PDF is selected based on a large dataset of no-stimulus data. The Scipy library is used to determine the maximum likelihood estimation (MLE) parameters for the chosen PDF. A gamma distribution was identified as the best fit for the no-stimulus histograms, as further discussed in the results chapter.

```
# Calculate shape, scale and location of gamma distribution
parameters_g = st.gamma.fit(freq_sig_base_val[i])
# Calculate gamma pdf
fitted_pdf = st.gamma.pdf(x, parameters_g[0], parameters_g[1],
parameters_g[2])
```

A large set of stimulus values was collected, and the means and standard deviations were normalized. By examining the relative means and standard deviations of the FFT magnitudes at the SSVEP frequencies, both with and without the stimulus present, we can generate an expected PDF for the FFT magnitudes when the stimulus is present, based on 30 seconds of no-stimulus data. This results in five no-stimulus PDFs and five stimulus PDFs, each corresponding to a different stimulus frequency. To calculate the probability that the user is focused on a stimulus, a naïve Bayes classifier can be applied. This task is more complex than the example in section 2.2.7, as there are now six possible classes, rather than just two. For simplicity, the calculations can be broken down into two scenarios: whether the user is looking at stimulus X or not. While the prior probability ($p(C_k)$) is unknown, it can initially be set to 0.5, assuming an equal likelihood of the user either attending or not attending to the stimulus.

$$p(LS|x) = \frac{p(x|LS) * p(LS)}{p(x|LS) * p(LS) + p(x|NLS) * p(NLS)} \quad (17)$$

LS *Looking at stimulus*
NLS *Not looking at stimulus*

This process can be repeated for each of the five stimulus frequencies, and the highest probability, provided it exceeds a defined threshold, can be used to determine whether the user is currently attending to a stimulus. If none of the probabilities for any of the stimuli exceed the threshold, it is more likely that the user is not focused on a stimulus. The threshold value would need to be carefully selected, but it should be set above 0.5, ensuring that the presence of a stimulus is considered more probable than the absence of one.

While a more sophisticated calculation could incorporate all classes simultaneously, such an approach would require more development time. Due to time constraints, this more complex method was not implemented or validated within the scope of the project.

Instead, a simpler approach was implemented and briefly tested during the data collection phase. At the time of implementation, sufficient no-stimulus data was available to select an appropriate PDF. However, there was insufficient stimulus data to define a stimulus-specific PDF. The simpler method involved recording a baseline for 30 seconds and using this data to calculate a complementary cumulative density function (CCDF), also known as a survival function. This

$$F(x) = \Pr[X > x]$$

$$F(x) = 1 - \int_{-\infty}^x f(\mu) d\mu \quad (18)$$

Pr[X>x] *Probability that a value is greater than x of a PDF*
f(μ) *Normalised likelihood at μ of a PDF*

function can be expressed as either:

A threshold probability of 0.1 was chosen, meaning that if the FFT magnitude at a stimulus frequency had less than a 10% likelihood of occurring under no-stimulus conditions, it was considered potentially caused by a stimulus. Additionally, if two consecutive FFT magnitudes at the same stimulus frequency exceeded this threshold, the corresponding checkbox for that stimulus was selected. This method was briefly tested, and when a stimulus was detected, it was correctly identified approximately 30% of the time when the stimulus was present. Out of five possible stimulus frequencies, the correct stimulus was selected about 50% of the time.

This approach was implemented in the basic alpha wave BCI described in the next chapter. However, it was ultimately concluded that this method was not suitable for SSVEP detection, and further development on this technique was discontinued.

4.1 SIGNAL PROCESSING

The raw signal captured in EEG-based Brain-Computer Interface (BCI) systems often contains various forms of noise and artifacts. These disturbances can originate from several sources, including the electrodes used to record the signal, the cables connecting the electrodes to the recording device, and the circuit board. Additionally, environmental factors, such as electromagnetic interference, can further degrade the signal quality. Noise and artifacts can significantly affect the accuracy of the analysis and the performance of the BCI system. Therefore, signal processing is a critical step in ensuring that the data used for feature extraction and classification is as clean and representative of brain activity as possible.

To address these challenges, multiple filtering techniques are employed to improve the signal quality by reducing or eliminating noise and artifacts. Three primary filters are used:

1. **Bandpass Filter (0-30 Hz):** The bandpass filter is designed to allow frequencies within a specific range to pass through while attenuating frequencies outside this range. In the context of EEG signals, the bandpass filter is typically set to pass frequencies between 0 and 30 Hz. This range includes the most relevant EEG frequency bands, such as delta, theta, alpha, and beta waves, which are essential for analyzing brain activity. By filtering out frequencies outside this range, the bandpass filter helps isolate the meaningful components of the EEG signal while removing low-frequency drifts and high-frequency noise.

2. **Notch Filter (50 Hz):** The notch filter is used to eliminate specific frequency components that contribute to noise in the signal. A common source of such noise is powerline interference, which typically occurs at 50 Hz in many regions. This interference can significantly distort the EEG signal, masking important features of brain activity. The notch filter is precisely tuned to remove the 50 Hz frequency, effectively eliminating powerline noise and allowing the rest of the signal to be analyzed without interference.
3. **Common Average Reference (CAR) Filter:** The CAR filter is a spatial filter that reduces noise by averaging the signals from all electrodes and subtracting this average from each individual electrode signal. This technique helps to minimize the impact of common-mode noise, which affects all electrodes equally, and enhances the detection of localized brain activity. By referencing each electrode to a common average, the CAR filter improves the signal-to-noise ratio, making it easier to detect relevant patterns in the EEG data.

These filtering methods are vital for preprocessing EEG signals before further analysis. By removing noise and artifacts, the filters ensure that the data fed into the feature extraction and classification stages of the BCI system is of high quality, leading to more accurate and reliable performance. Effective signal processing not only improves the functionality of the BCI system but also enhances the user experience by providing a more robust and responsive interface.

4.2 FEATURE EXTRACTION

The frequency-domain analysis of recorded EEG signals involves applying the Fourier transform to estimate the corresponding spectral details. The Fast Fourier Transform (FFT) is typically employed to analyze amplitude modulations at specific frequencies. This is achieved by plotting the frequency spectrum of the acquired EEG responses, allowing for the identification and tracking of significant frequency components within the signal.

In the time domain, the EEG signal is represented as a function of time, showing how the voltage fluctuates over time at each electrode. However, many of the important characteristics of EEG signals are more easily analyzed in the frequency domain, where the signal is broken down into its constituent frequencies. The FFT is a mathematical algorithm that efficiently performs this conversion, taking a sequence of time-domain samples and decomposing them into a sum of sinusoidal components at various frequencies.

The resulting frequency-domain representation provides a spectrum that highlights the amplitude of the signal at different frequencies. This spectral information is crucial because various brain activities are associated with specific frequency bands. For instance, alpha waves typically occur in the 8-13 Hz range and are associated with relaxation, while beta waves, found in the 13-30 Hz range, are linked to active thinking and focus. By analyzing these frequency components, the FFT allows for the extraction of features that are relevant to the classification and interpretation of mental states or cognitive tasks.

An input EEG signal $x(t)$ is sampled at N discrete time intervals to convert it into a discrete-time signal $x(n)$, consisting of a total of N samples. The resultant signal can then be analyzed using the Discrete Fourier Transform (DFT) or Fast Fourier Transform (FFT), which is mathematically defined by the following equation:

$$X(k) = \sum_{n=0}^{N-1} x(n) e^{-\frac{j2\pi kn}{N}}, \quad k = 0, 1, 2, \dots, N-1$$

where $X(k)$ represents FFT of finite duration signal $x(n)$ at the different frequency points given as $f=k/N$.

4.3 CLASSIFIER DESIGN

The extracted features, represented by the frequency spectrum of the EEG signal, are then classified using a machine learning model. In this case, a Convolutional Neural Network (CNN) is employed for classification. The CNN is well-suited for this task due to its ability to automatically learn and extract relevant patterns from the input data. By leveraging the frequency spectrum as input, the CNN can identify distinguishing features that correspond to different cognitive states or activities.

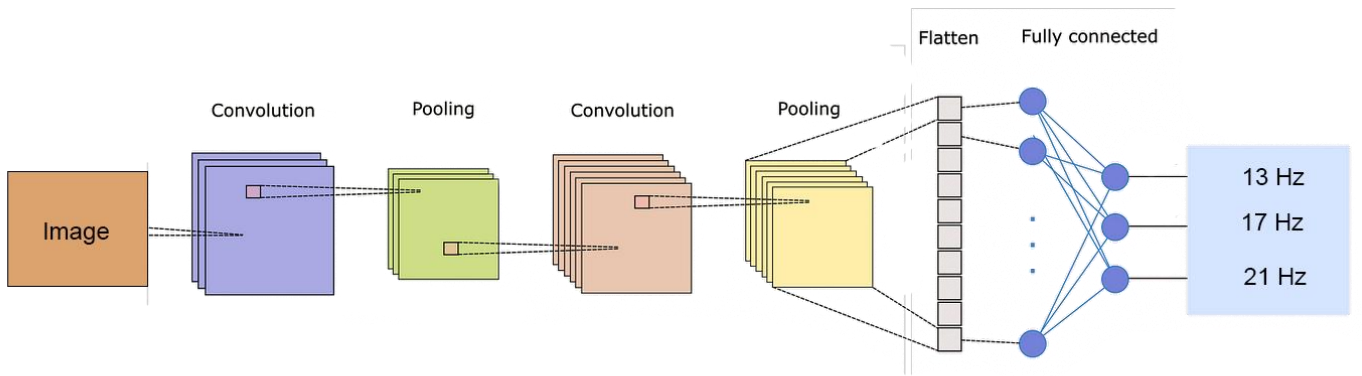


Figure 22: Example of a CNN Model Architecture.

In this project, the network consists of 10 layers, designed to effectively capture and process the features of the input data. The architecture of the network is as follows:

1. **Convolutional Layer:** This initial layer applies 64 filters, each of size (3×3) , to the input data. The layer utilizes the Rectified Linear Unit (ReLU) activation function, which introduces non-linearity and helps the network learn complex patterns within the data.
1. **Max Pooling Layer:** Following the convolutional layer, a max pooling layer with a (2×2) filter is applied. This layer reduces the spatial dimensions of the data, effectively down-sampling the input while retaining the most significant features.
2. **Convolutional Layer:** A second convolutional layer with 64 filters of size (3×3) is applied, again using the ReLU activation function. This layer further refines the feature extraction process.
3. **Max Pooling Layer:** Another max pooling layer with a (2×2) filter follows, continuing the

down-sampling process to reduce the data's dimensionality.

4. **Convolutional Layer:** The third convolutional layer, also with 64 filters of size (3×3) and ReLU activation, further processes the features extracted from the previous layers.
5. **Max Pooling Layer:** A final max pooling layer with a (2×2) filter is applied, further compressing the feature maps generated by the previous layer.
6. **Flatten Layer:** This layer transforms the 2D output of the previous layer into a 1D vector, making it suitable for input into the fully connected layers.
7. **Fully Connected (Dense) Layer:** The first dense layer consists of 128 neurons and utilizes the ReLU activation function. This layer integrates the features learned by the convolutional layers and begins to make high-level decisions.
8. **Fully Connected (Dense) Layer:** Another dense layer with 128 neurons and ReLU activation is included, further refining the network's ability to classify the data.
9. **Fully Connected (Dense) Layer:** The final layer consists of 3 neurons and uses the softmax activation function, which converts the network's output into a probability distribution over the three possible classes.

The network is trained using the Adam optimizer, which is known for its efficiency and ability to handle sparse gradients. The loss function used is sparse categorical cross-entropy, appropriate for multi-class classification problems with integer labels. The model is trained for 10 epochs, with 10% of the data reserved for validation. The batch size is set to 32, balancing the need for efficient training with the stability of the gradient updates.

This carefully designed CNN architecture is crucial for accurately classifying EEG signals, ensuring that the model can effectively learn and generalize from the provided data.

4.4 USER INTERFACE AND SOFTWARE DESIGN

After acquiring the raw EEG signals, it is essential to denoise the signal using the specified signal processing techniques before proceeding with classification using the trained CNN model. To facilitate this process, a comprehensive software solution is required to handle all stages, from signal processing to classification, while also providing an interface for user interaction.

In the proposed method, the software should include a user interface featuring three flickering bulbs. When the user focuses on a particular flickering bulb, their brain signals change correspondingly. The captured raw EEG signals are then provided to the software, which processes them using the implemented denoising techniques and classifies the signals using the trained CNN model. Based on the classification results, the software should then react accordingly, executing the appropriate response.

This software must integrate seamlessly with the hardware components and allow for real-time interaction with the user. The design should prioritize user-friendly features, ensuring that the interface is intuitive and responsive.

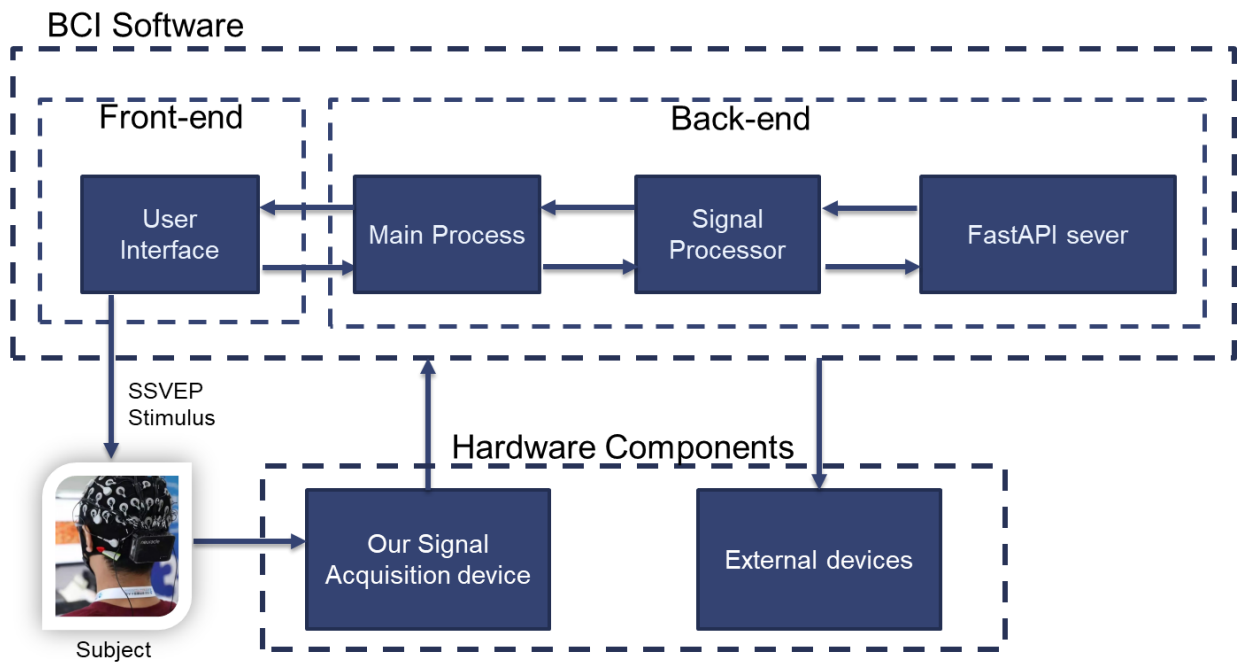


Figure 23: Block Diagram of the System Structure

The software system is divided into two primary components: the front end and the back end.

To develop the system, the Electron.js framework, along with JavaScript, was utilized for

designing the front-end interface. The back-end functionality was implemented using Python programming, ensuring efficient processing and communication between the user interface and the core system components.

The front end is responsible for user interaction, providing a user-friendly interface for controlling the system.

The back end handles the core operations and is further divided into three main parts:

1. **Main Process:** This component facilitates communication between the user interface and other back-end processes. It acts as the central hub, ensuring seamless interaction between different parts of the system.
2. **Signal Processor:** The signal processor performs all the necessary signal processing tasks. It prepares the EEG data by filtering and extracting features, making it ready for input into the machine learning model for prediction.
3. **FastAPI Server:** The FastAPI server takes the processed signals from the signal processor as input, runs the machine learning model to predict outcomes, and returns the results to the main process for further action.

4.5 Integration with External Devices

After the signal is classified, a control signal must be sent to an external device to address the needs of the disabled person. To accomplish this, software must be developed to integrate with a microcontroller. The output of the software is processed by the microcontroller, and the appropriate control signal is sent to the external device. In this project, an Arduino board is being used for this purpose. Therefore, the serial port must be enabled in the BCI software to allow input to be provided to the Arduino board.



Figure 24: Schematic Diagram Illustrating External Device Control Functionality

4. RESULTS

In this section, we will discuss the results obtained from each phase outlined in the methodology section. The outcomes from signal acquisition, signal processing, feature extraction, classifier design, and user interface development are presented and analyzed in detail.

4.1 SIGNAL ACQUISITION

The EEG acquisition circuit was designed using LTSpice, and simulations were conducted to analyze its performance. The simulated frequency responses of both the circuit output and the driven right leg (DRL) circuit were obtained and are shown in Figure 24 (Simulated Frequency Response of Circuit Output) and Figure 25 (Simulated Frequency Response of the Driven Right Leg).

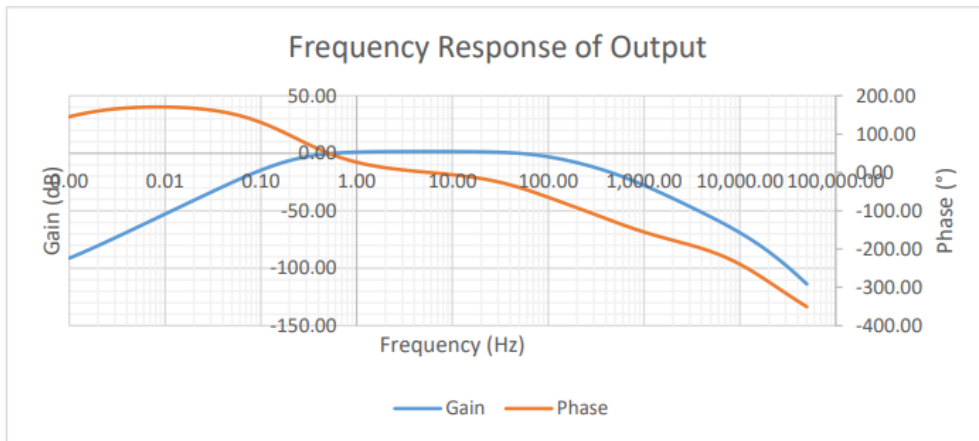


Figure 25: Simulated frequency response of circuit output from a differential input of $50 \mu V$

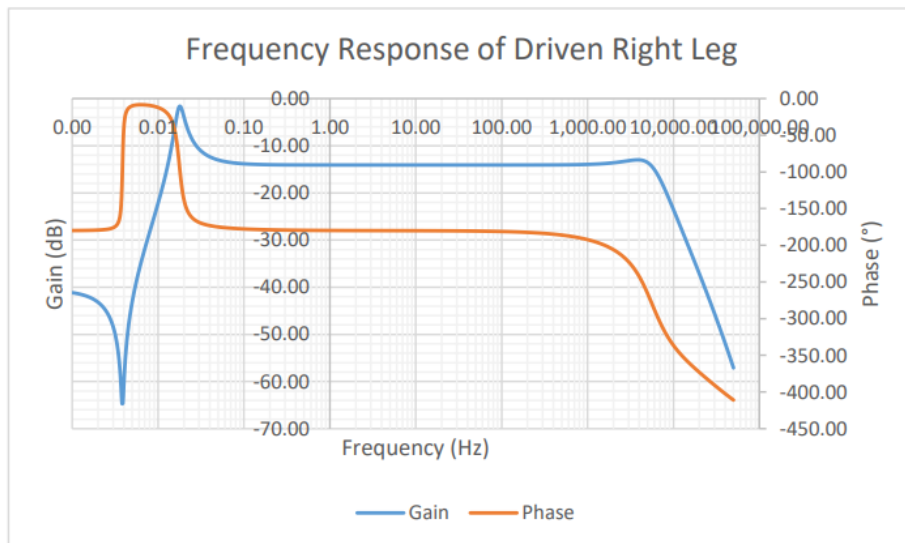


Figure 26: Simulated frequency response of driven right leg from a common mode input of $200 mV$

After the simulation, the circuit was constructed and tested under the same conditions used during simulation. The output of the circuit and the DRL circuit were measured, and these measured values were plotted alongside the simulation results on the same graphs, as shown in Figure 20 (Frequency Response of Circuit Output – Simulated and Measured) and Figure 21 (Frequency Response of DRL – Simulated and Measured).

The results indicate that the measured values closely align with the simulated values. This consistency confirms that the circuit performed as intended within the desired frequency range for acquiring SSVEP-based EEG signals.

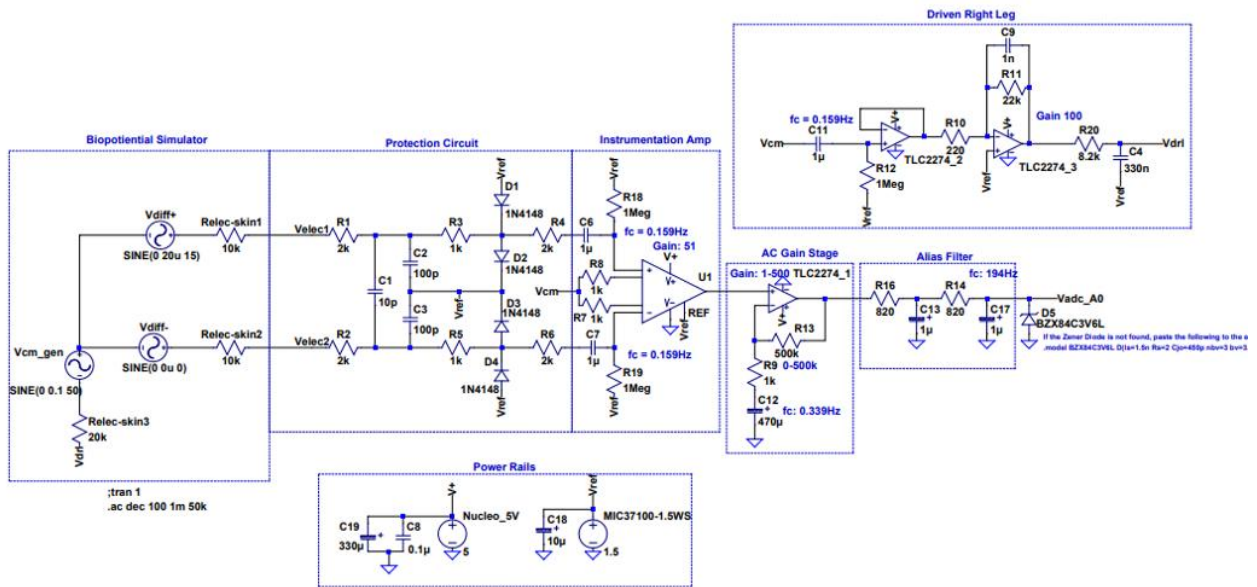


Figure 27: LTspice EEG measurement circuit diagram

4.2 Measuring Alpha Waves

The next test aimed to evaluate the circuit's ability to measure and amplify EEG signals while minimizing 50 Hz interference. Alpha waves, which are relatively easy to elicit, were chosen for this test. The user modulated their alpha wave activity by alternating between opening and closing their eyes. As alpha waves are most prominent in the occipital lobe [27], the positive and negative electrodes were placed at O1 and O2. These locations were also chosen because they are close to each other, allowing the wires to be tightly twisted up to the electrodes, reducing the risk of electromagnetic interference (EMI) on the wires.

The test procedure was as follows:

- i. The DRL electrode was attached to the right mastoid using an ECG pad.
- ii. Nuprep abrasive gel was applied to O1 and O2 to remove oils and dead skin, lowering the electrode-skin impedance.
- iii. Two low-cost electrodes were filled with Signa gel.
- iv. The electrodes were placed on O1 and O2 and secured in place using a swimming cap.
- v. The test began with the user keeping their eyes open for 60 seconds.
- vi. The user then closed their eyes for 30 seconds to elicit an alpha wave response.

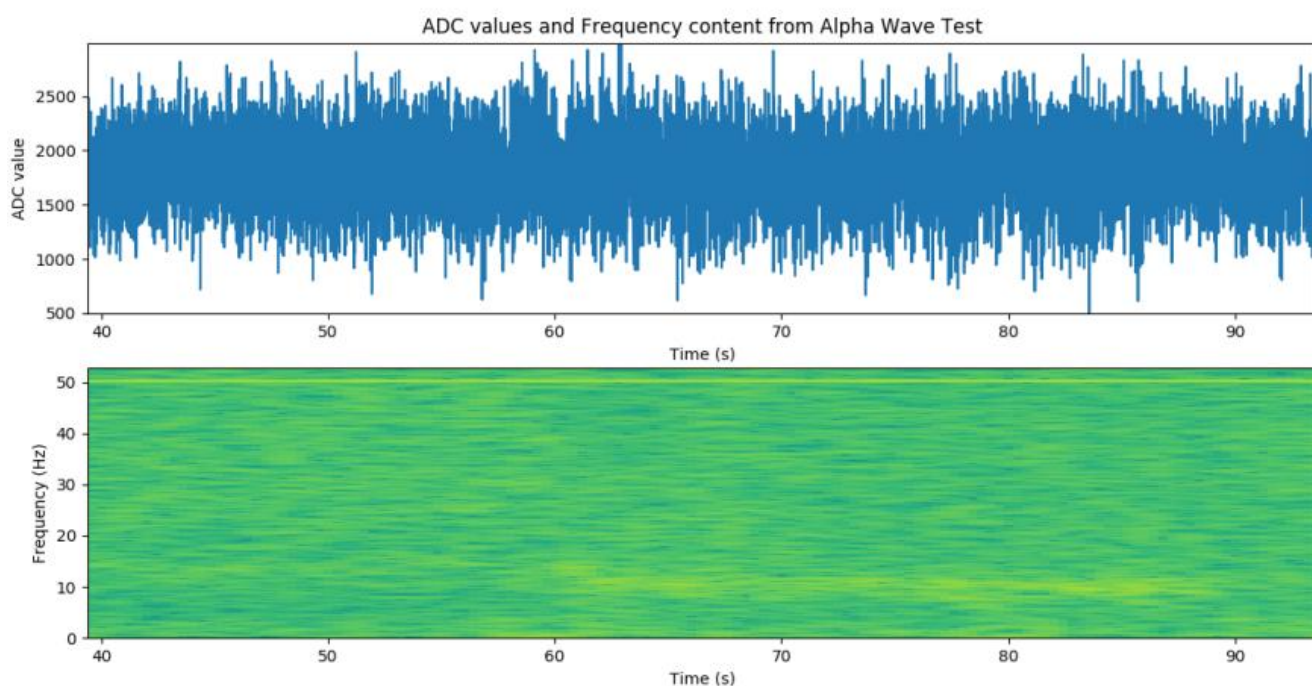


Figure 27: Time-domain signal and spectrogram of EEG recorded between O1 and O2. The user kept their eyes open from 0 to 60 seconds, closed them from 60 to 90 seconds, and reopened them for the remainder of the recording. In the spectrogram, a distinct yellow line appears around 10 Hz during the 60 to 90-second interval, indicating an increase in alpha wave activity.

The spectrogram in Figure 38 illustrates the frequency content of the EEG signal over time. Around the 60-second mark, a noticeable increase in activity at approximately 10 Hz (visible as a yellow line from 60 to 90 seconds) corresponds to the user closing their eyes. A persistent 50 Hz signal, indicative of powerline interference, is present throughout the test. A video recording of the real-time plot was captured, and the real-time FFT also demonstrated an increase in activity around 10 Hz at the 60-second mark, confirming that the EEG's frequency content can be processed in real-time.

4.4 Fitting Probability Density Functions

To create an accurate model for the method described in section 3.2.2.3, a large dataset was necessary. The data was collected by presenting the user with a single large checkerboard box flashing at a specific frequency, as shown in Figure 28.

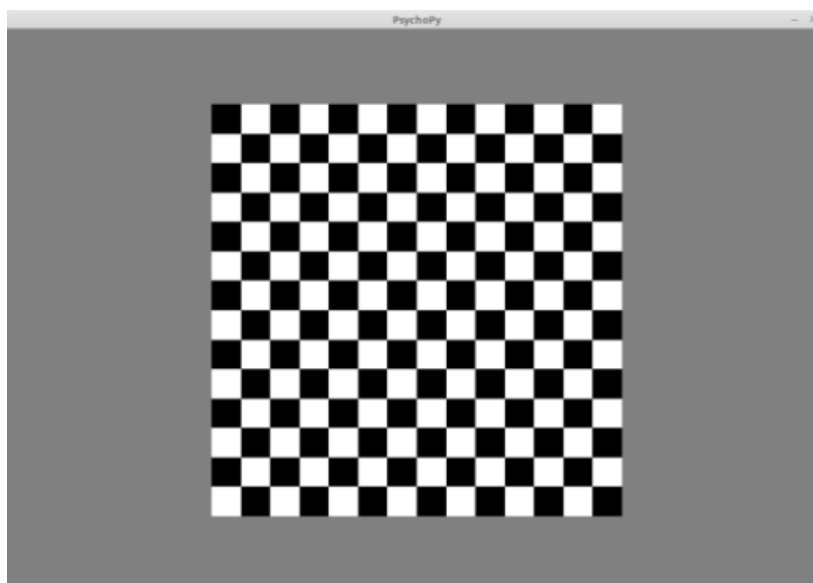


Figure 28: Single large flashing checkerboard used to elicit SSVEP responses.

Test Procedure

The following steps were carried out during the test:

- 1) The DRL electrode was attached to the right mastoid, and the negative electrode was attached to the left mastoid, both secured with ECG pads.
- 2) Nuprep abrasive gel was applied to the Oz electrode site to remove oils and dead skin, reducing electrode-skin impedance.
- 3) A low-cost electrode was filled with Signa gel.
- 4) The electrode was placed on Oz and secured using a swimming cap.
- 5) The test began with the user staring at a blank screen for 30 seconds to record a no-stimulus baseline.
- 6) The user then focused on a single large checkerboard stimulus flashing at a specific frequency for 120 seconds to collect stimulus data.

This procedure was repeated for all five frequencies used in the main application. The Oz electrode site was chosen because it is known to produce the strongest SSVEP responses [27]. Initial tests measuring between O1 and O2 did not show any SSVEP activity, leading to the decision to use Oz.

All collected data were validated through two methods:

1. Two FFTs were plotted, one for the entire no-stimulus period and another for the entire stimulus period, to check for a peak at the stimulus frequency in the stimulus data compared to the no-stimulus data.
2. A spectrogram of the entire test, including both the no-stimulus and stimulus periods, was plotted to confirm the presence of the stimulus frequency during the time the user was focused on the stimulus.

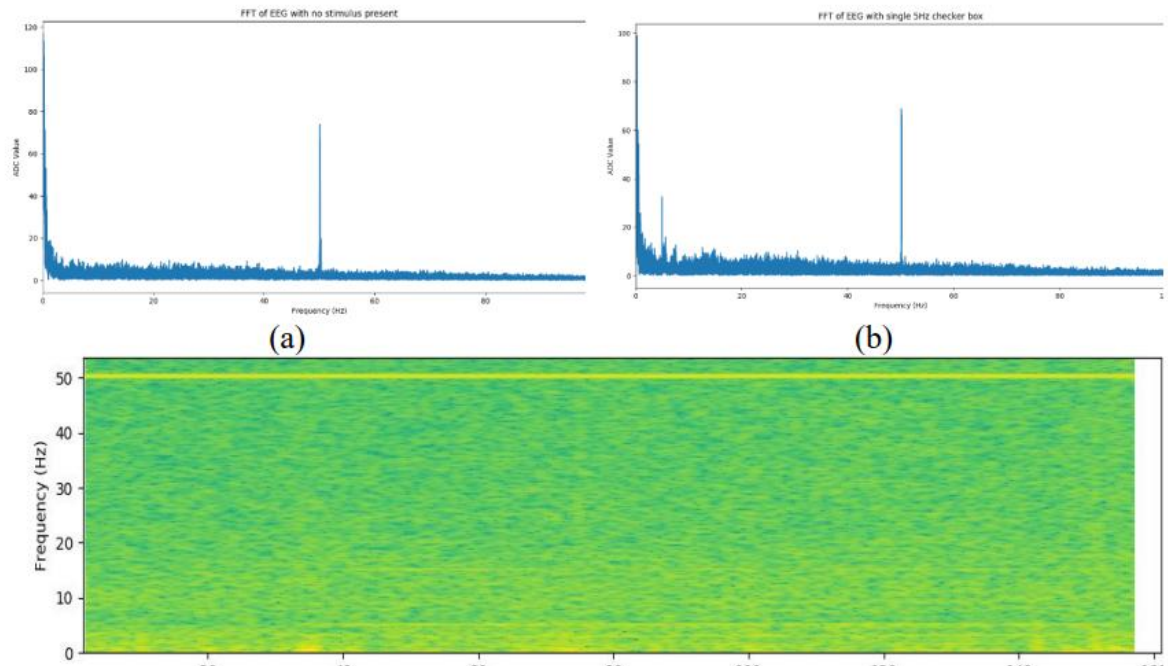


Figure 29: (a) FFT of EEG during the no-stimulus period. (b) FFT of EEG with a 5 Hz stimulus, showing a clear spike at 5 Hz. (c) Spectrogram of EEG with a 5 Hz stimulus, where a faint yellow line appears at 5 Hz from approximately 35 seconds onwards, indicating the onset of the stimulus.

This test was demanding over multiple trials, so the full dataset was collected across several sessions. Since the data collection spanned multiple sessions, variations in gain settings, electrode-skin impedance, and interference could affect the magnitude distribution between tests. To address this, the results were normalized to enable comparison and combination. Normalization was achieved by calculating the mean FFT magnitude of each SSVEP frequency during the no-stimulus period for each session. All FFT magnitudes from that session were then normalized to this no-stimulus mean.

In total, 1016 seconds of data were used to create the no-stimulus histograms, and 761 seconds of data were used for the stimulus histograms. Five different probability density functions (PDFs) were evaluated against the histograms. The evaluation involved visual inspection to assess the match and calculating the negative log-likelihood function (NNLF) values using Scipy to determine the best-fitting PDF.


```

# Find the pdf which yields smallest negative loglikelihood function
# Code from stack overflow - Martin
distributions = [st.norm, st.rayleigh, st.gamma, st.chi, st.lognorm]
nnlfs = []
for distribution in distributions:
    pars = distribution.fit(buff)
    nnlf = distribution.nnlf(pars, buff)
    nnlfs.append(nnlf)
results = [(distribution.name, nnlf) for distribution, nnlf in
zip(distributions, nnlfs)]
    = sorted(zip distributions nnlfs), key=lambda d: d[1])[0]
print "Best fit reached using {}, NNLF value:
{}".format(best_fit[0].name, best_fit[1]))

```

The 12 Hz no-stimulus histogram with five fitted PDFs is shown in Figure 30.

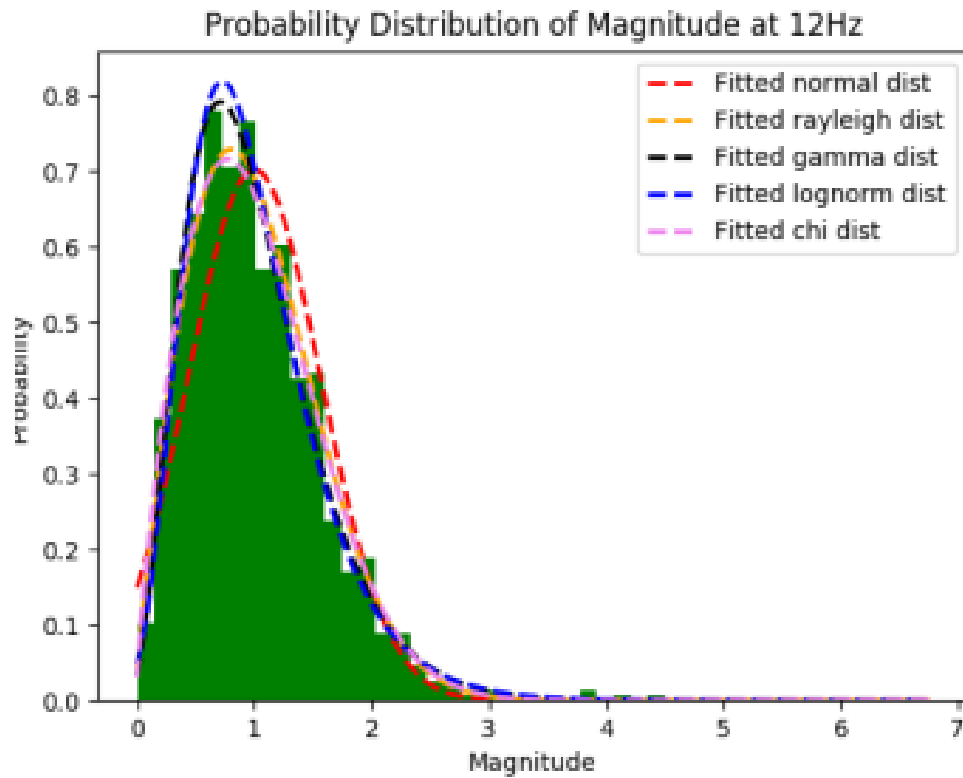


Figure 30: Histogram of normalized FFT magnitudes of EEG at 12 Hz (no-stimulus) with fitted probability density functions (PDFs).

The gamma distribution (black) and the log-normal distribution (blue) closely matched the histogram, with the gamma PDF producing the smallest NNLF value. For all frequencies except 5 Hz during the no-stimulus condition, the gamma PDF yielded the lowest NNLF. At 5 Hz, the log-normal PDF provided a slightly better fit than the gamma PDF. However, the gamma PDF was selected to model the no-stimulus data overall, as it provided the best fit across all frequencies. The 12 Hz stimulus histogram with five fitted PDFs is presented in Figure 43.

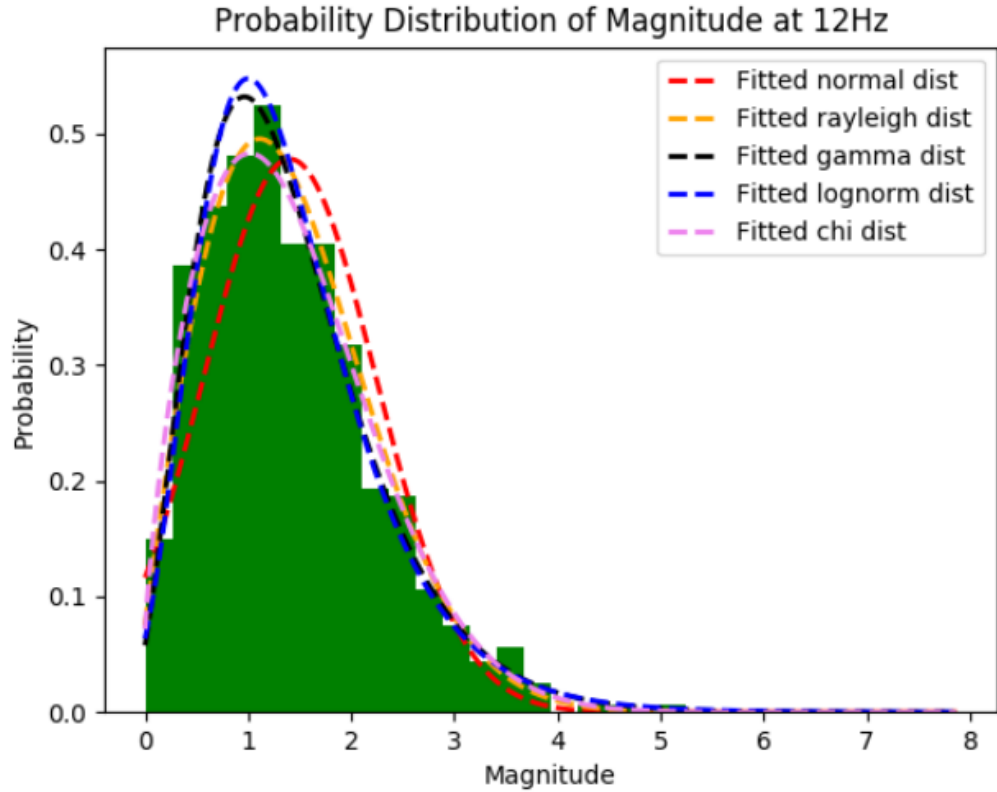


Figure 30: Histogram of normalized FFT magnitudes of EEG at 12 Hz (with 12 Hz stimulus) along with fitted probability density functions (PDFs).

The chi distribution (pink) yielded the smallest NNLF for all stimulus histograms and was therefore chosen to model the FFT magnitudes in the presence of a stimulus. All histograms with their fitted PDFs are provided in Appendix G – Histograms and Probability Density Functions, and the code used to generate the histograms and PDFs is included on the CD at the back of the appendix. The mean and standard deviation for each histogram were calculated and are presented in Table 3.

Table 3: Normalized means and standard deviations for no-stimulus and stimulus histograms.

Frequency (Hz)	No-stimulus		Stimulus	
	Mean	Standard	Mean	Standard
	Deviation		Deviation	
5	1	0.63	1.71	0.81
10	1	0.57	1.23	0.65
12	1	0.57	1.40	0.83
15	1	0.53	1.39	0.75
20	1	0.57	1.55	0.88

The mean values for all stimulus data are higher than those for no-stimulus data, as expected. However, the larger standard deviation observed in most stimulus data indicates that the PDFs for stimulus data are more spread out. This increased spread may result in less separation from the no-stimulus PDFs, making it more challenging to differentiate between stimulus and no-stimulus values using a naïve Bayes classifier.

To evaluate the separation between the distributions, the fitted PDFs for each frequency were plotted for both no-stimulus and stimulus conditions. The 5 Hz frequency exhibited the best separation, as shown in Figure 31.

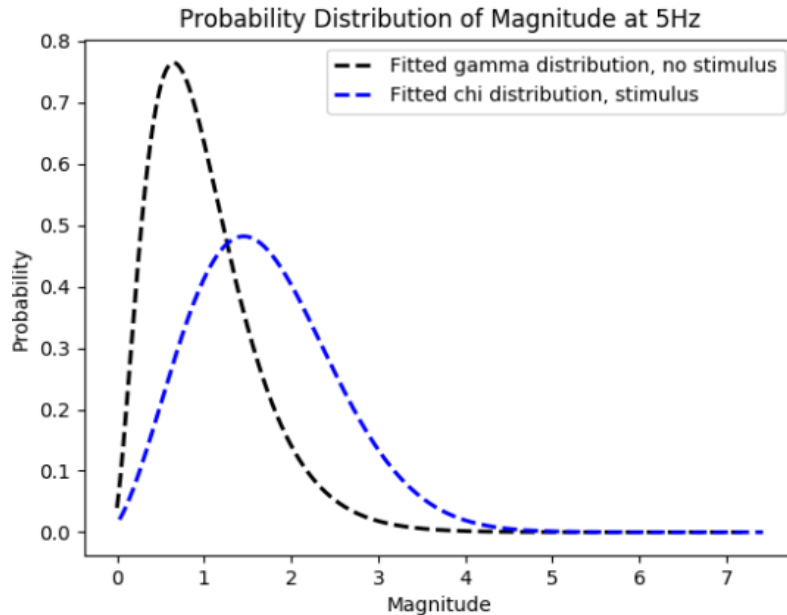


Figure 31: Normalized probability density functions (PDFs) of FFT magnitudes of EEG at 5 Hz, showing no-stimulus (black) and 5 Hz stimulus (blue) conditions.

The 5 Hz PDFs demonstrate good separation, suggesting it may be feasible to compare the probabilities of the two PDFs to detect the presence of an SSVEP stimulus. By utilizing the calculated means and

standard deviations, along with a baseline recording of no-stimulus data, it could be possible to construct the expected stimulus PDF for each frequency. This would enable a statistical determination of the presence of an SSVEP. This approach assumes that the calculated means and standard deviations remain consistent across different users and tests, accurately representing the FFT magnitudes associated with SSVEP stimuli.

However, due to time constraints, the proposed method for SSVEP stimulus detection and the full BCI software were not tested on users.

4.3 SIGNAL PROCESSING

To proceed with the remaining components of the project prior to completing the signal acquisition, it was necessary to use an EEG dataset for training the machine learning model to classify the signals. Initially, we did not have access to raw EEG signals; therefore, we sourced a dataset from GitHub (Source: sylvchev / dataset-ssvep-led).

This dataset includes raw EEG signals corresponding to three flickering frequencies: 13 Hz, 17 Hz, and 21 Hz. For each flickering frequency, 160 trials were recorded, with each trial lasting 5 seconds. The data were sampled at a rate of 256 Hz.

The signals were recorded using eight electrodes, placed according to the 10-20 system at the following positions: Oz, O1, O2, POz, PO3, PO4, PO7, and PO8. For our analysis, only the signals from the Oz electrode were utilized.

After applying filters to the raw EEG signals, the resulting filtered signals were obtained. Figure 27

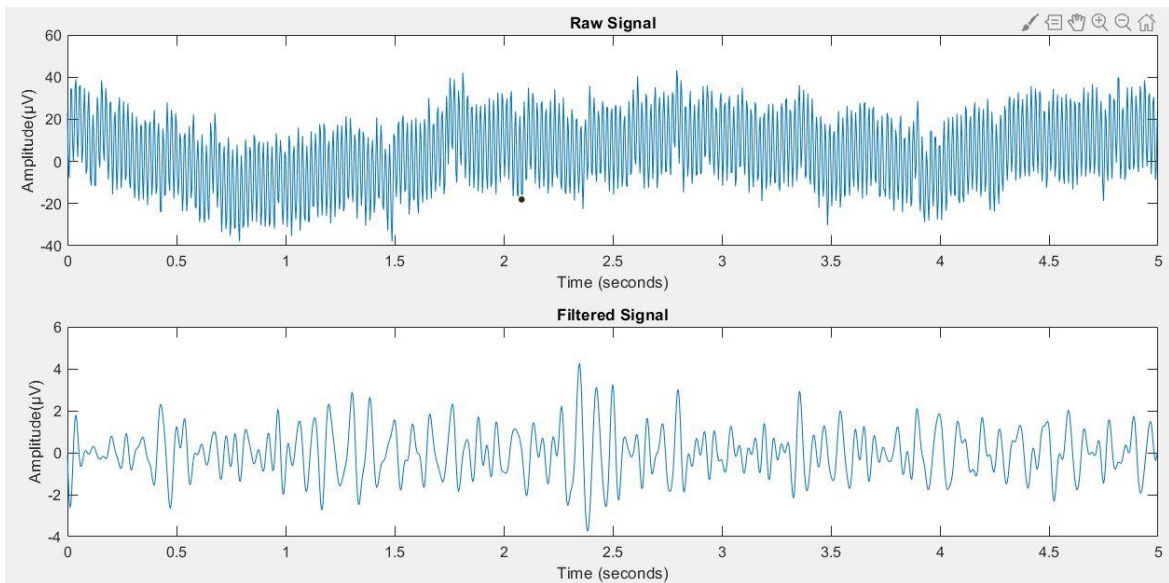


Figure 28: An Example of an EEG raw and Filtered Signal Based on a 13 Hz Stimulus.

presents an example of both the raw and filtered signals, corresponding to the 13 Hz stimuli. For the three flickering frequencies in the dataset, a total of 480 filtered signals were generated, each with a duration of 5 seconds.

4.4 FEATURE EXTRACTION

The 480 filtered signals were subsequently subjected to the Fast Fourier Transform (FFT), resulting in 480 corresponding spectrums.

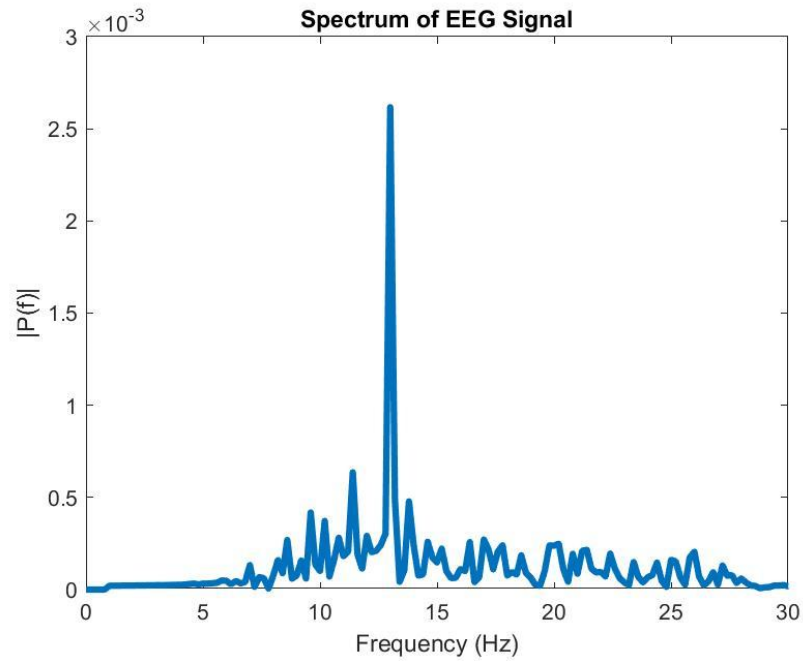


Figure 30: An Example of FFT Spectrum of filtered signal based on a 13 Hz Stimulus.

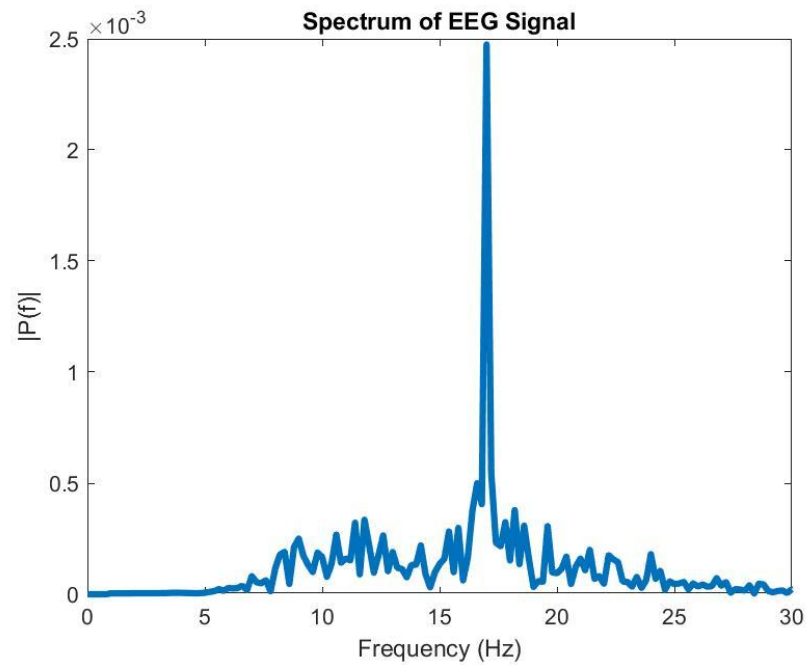


Figure 29: An Example of FFT Spectrum of filtered signal based on a 17 Hz Stimulus.

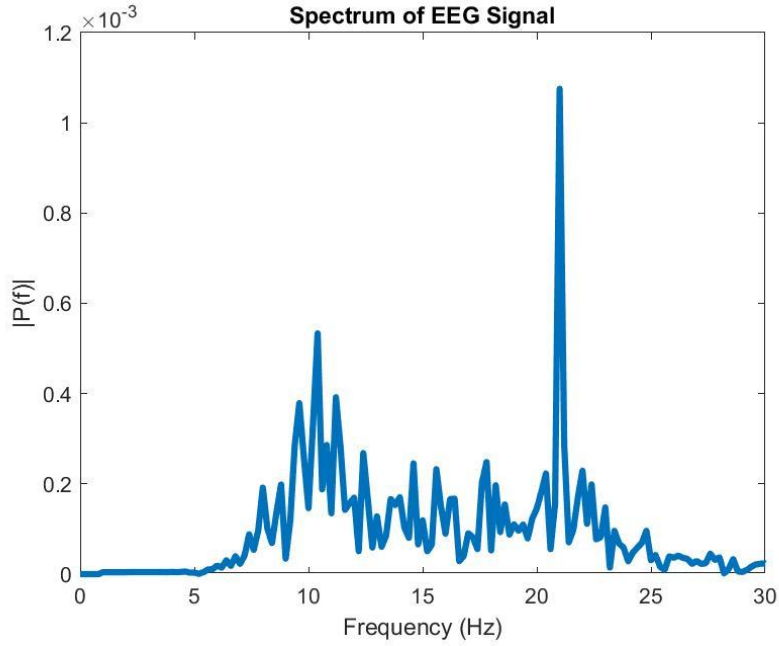


Figure 31: An Example of FFT Spectrum of filtered signal based on a 21 Hz Stimulus.

Upon examining the frequency spectra (Figures 28, 29, and 30), significant magnitudes were observed near 13 Hz, 17 Hz, and 21 Hz, confirming that the signals correspond to stimuli based on these frequencies. This characteristic is utilized to classify the signals into their respective categories.

4.5 CLASSIFIER DESIGN

To evaluate the performance of the Convolutional Neural Network (CNN) model during training, accuracy was used as the primary metric. After training the model for 10 epochs, the following results were achieved:

- Training accuracy: 1.0
- Training loss: 0.0015
- Validation accuracy: 0.9375
- Validation loss: 0.1615

These results indicate that the model performed exceptionally well on the training data, with a perfect accuracy score. The validation accuracy of 0.9375 demonstrates strong generalization on

unseen data, although some slight overfitting may be indicated by the difference between training and validation loss.

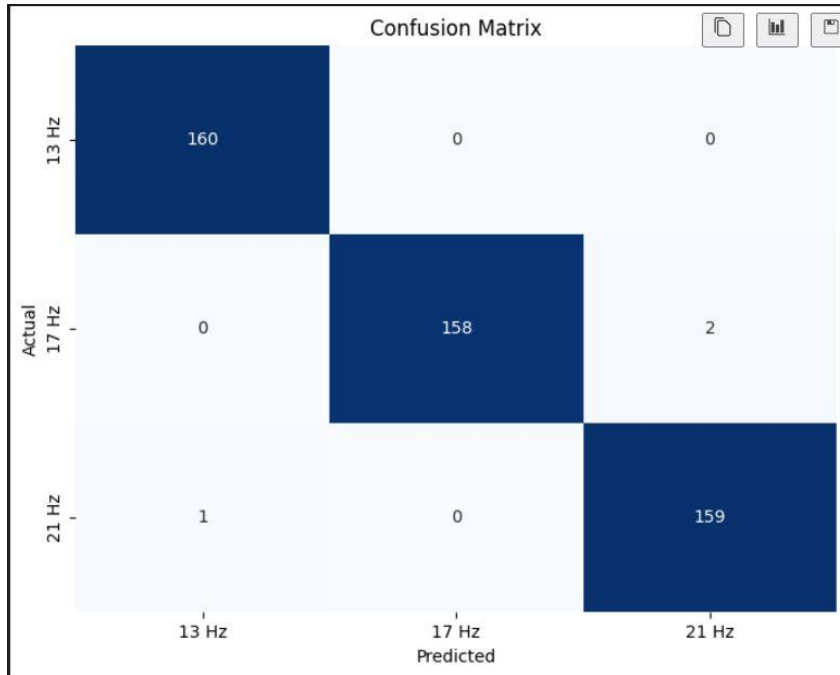


Figure 33: Confusion Matrix of the CNN model

Additionally, **Figure 31** presents the confusion matrix generated after model evaluation. The

	precision	recall	f1-score	support
13 Hz	0.99	1.00	1.00	160
17 Hz	1.00	0.99	0.99	160
21 Hz	0.99	0.99	0.99	160
accuracy			0.99	480
macro avg	0.99	0.99	0.99	480
weighted avg	0.99	0.99	0.99	480

Figure 32: Classification report of the CNN model

confusion matrix indicates that the CNN model is highly accurate, with minimal misclassification across the three frequency classes. The model performs exceptionally well for both the 13 Hz and 21 Hz classes, with only slight confusion between the 17 Hz and 21 Hz classes. These results suggest that the model can reliably distinguish between the different SSVEP frequencies with a high degree of accuracy.

Figure 32 displays the classification report, providing further insights into precision, recall, and F1-score metrics for each class. This detailed analysis highlights the robustness and reliability of

the CNN model in classifying EEG signals based on the given stimuli frequencies.

4.6 USER INTERFACE AND SOFTWARE DESIGN

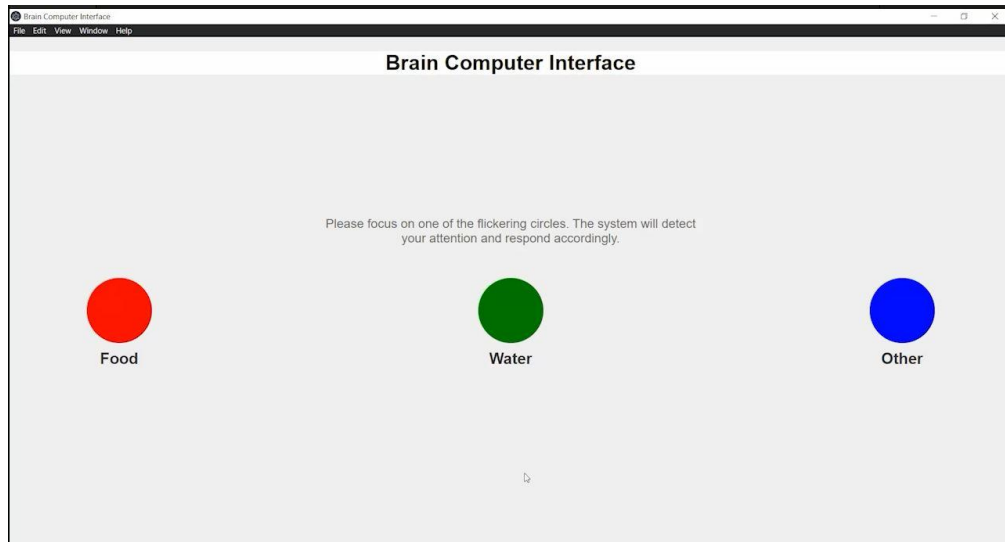


Figure 34:BCI interface

Figure 33 shows the user interface developed using the Electron.js framework. the interface features three bulbs (red, green, and blue), each flickering at 13 Hz, 17 Hz, and 21 Hz, respectively. The user is required to focus on a specific bulb according to their preference.

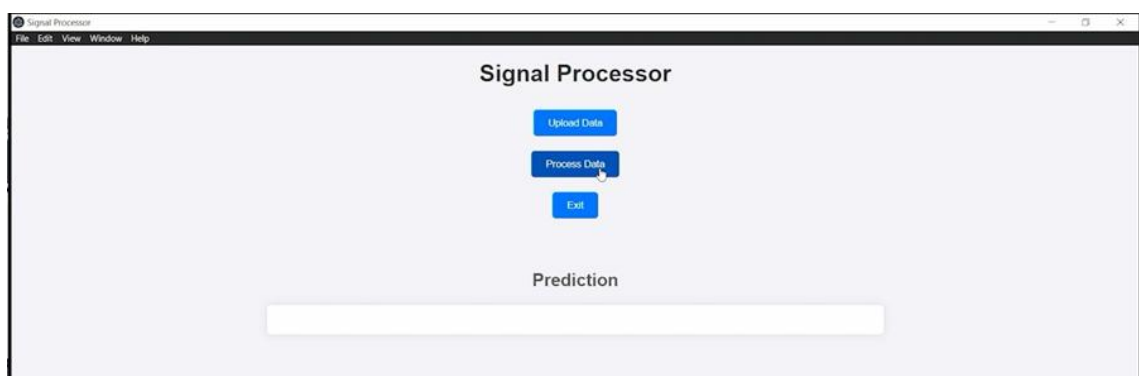


Figure 35: Signal Processing Interface

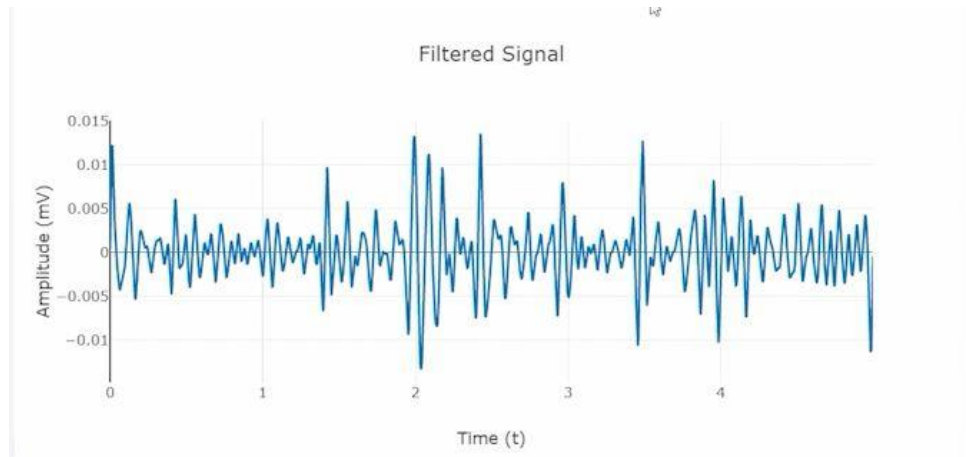


Figure 36: Filtered signal displayed by the software

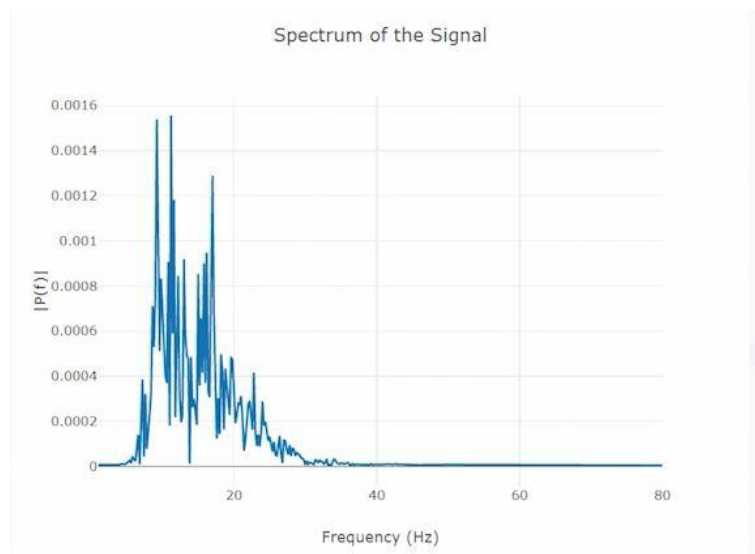


Figure 38: FFT Spectrum displayed by the software

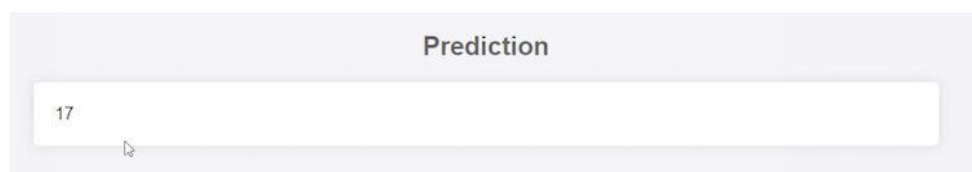


Figure 37: The classification of the signal displayed by the software

Figure 34 illustrates the signal processing interface developed for internal testing purposes. This interface is not intended for user interaction. It allows for the importation of raw EEG signals, and upon pressing the "Process Data" button, the software performs all necessary filtering, feature extraction, and classification, subsequently displaying the signal class. However, this process should ideally be real-time, eliminating the need for manual data importation by the user. Furthermore, the output displayed by this interface is not yet connected to control signals for external devices; integration with external device operation will be necessary based on the classified results.

4.7 INTEGRATION WITH EXTERNAL DEVICES

In this setup, an Arduino board, a breadboard, and three LEDs are used. The three LEDs are assumed to represent the external devices. Control signals are sent from the Arduino board to the LEDs (external devices) to address the needs of the disabled person. The red, green, and yellow LEDs are associated with 13 Hz, 17 Hz, and 21 Hz frequencies, respectively.

For example, if the disabled person focuses on the 13 Hz flickering bulb displayed on the screen, the BCI software outputs the value 13 to the Arduino board. The control signal is then sent by the Arduino board to turn on the red LED.

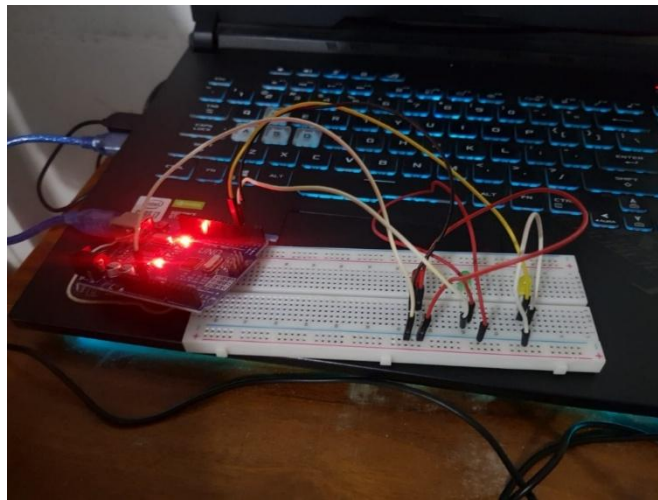


Figure 40: External devices control mechanism

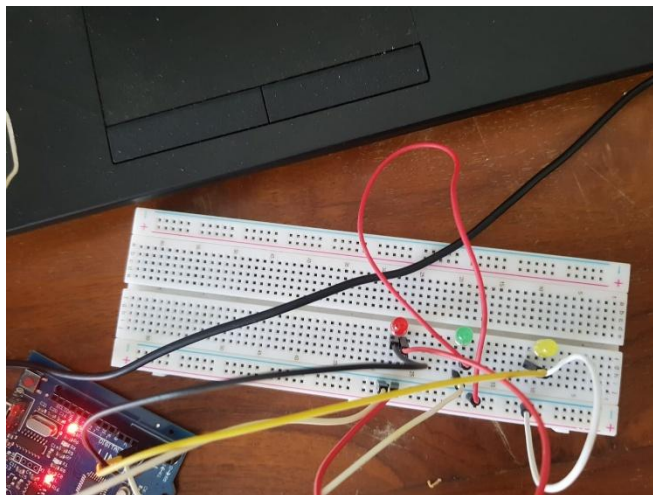


Figure 39: Three LEDs are assumed to be three external devices.

If the three bulbs are replaced with three external devices, those external devices can be integrated into the system. In this case, the system will send control signals to these external devices, enabling them to perform the required actions based on the needs of the user

5. DISCUSSION

One of the key limitations in our current system design is the use of a single-channel EEG for signal acquisition. While this approach simplifies hardware complexity and reduces cost, it inherently impacts the overall accuracy of the system. Multi-channel EEG systems generally provide richer data by capturing signals from different regions of the brain, thus allowing for better spatial resolution and more robust feature extraction. In contrast, single-channel systems may suffer from reduced signal fidelity and increased noise sensitivity, which can affect the classification accuracy. This trade-off between system complexity and accuracy is a notable factor in our design, and future work may involve exploring multi-channel setups to improve performance.

Another challenge faced in our system is the integration between the front-end and back-end components. The front end of the system is developed using JavaScript (Electron.js), while the back end is implemented in Python for signal processing and classification. This cross-platform architecture, while flexible and suitable for rapid prototyping, introduces additional overhead in terms of communication between the two layers. JavaScript, being an interpreted language, adds latency in executing client-side tasks, while Python's processing, especially in handling large datasets such as EEG signals, can be computationally intensive. The need for continuous data transfer and synchronization between these two languages results in increased processing time, which could affect real-time performance.

6. CONCLUSION

In this project, we have successfully completed the signal processing, feature extraction, and classifier design components. Currently, we are in the process of developing the signal acquisition module and user interface design. Additionally, integration with external devices and the testing phase are still pending.

At present, the system does not support real-time signal processing, and the software is not yet customizable for users. In the final version of the software, users will have the ability to modify the application according to their preferences, ensuring a more flexible and personalized experience.

Several limitations were identified during the development process. For instance, the use of a single-channel EEG, although cost-effective, has resulted in reduced accuracy compared to multi-channel systems, which provide better spatial resolution and improved data fidelity.

Future work could focus on enhancing the system's performance and accuracy by exploring the use of multi-channel EEG systems, which would allow for more comprehensive data collection and improved signal processing capabilities.

7. REFERENCES

- [1] M. Clinic. (2016, January 16). Brain Anatomy, Anatomy of the Human Brain. Available: <http://www.mayfieldclinic.com/PE-AnatBrain.htm>
- [2] M. G. N. Garcia, T. K. TSONEVA, D. BALDO, D. Zhu, P. H. A. GABRIELSSON, and K. P. N.V., "Device and method for cognitive enhancement of a user," 2014. Available: <https://www.google.com/patents/EP2681729A1>.
- [3] L. Haas, "Hans Berger (1873–1941), Richard Caton (1842–1926), and electroencephalography," (in eng), Journal of Neurology, Neurosurgery, and Psychiatry, vol. 74, no. 1, p. 9, Jan 2003.
- [4] S. N. Abdulkader, A. Atia, and M.-S. M. Mostafa, "Brain computer interfacing: Applications and challenges," Egyptian Informatics Journal, vol. 16, no. 2, pp. 213-230, 2015/07/01/ 2015.
- [5] imotions. (2017). EEG Headset Prices – An Overview of 15+ EEG Devices. Available: <https://imotions.com/blog/eeg-headset-prices/>
- [6] T. O. Project. The ModularEEG. Available: <http://openeeg.sourceforge.net/doc/modeeg/modeeg.html>
- [7]] PenBCI. Ganglion Board (4-channels). Available: <https://shop.openbci.com/products/pre-order-ganglion-board>
- [8] E. V. Hippel, Open Source Software: Innovation By and For Users – No Manufacturer Required!: Massachusetts Institute of Technology, 2003. [Online]. Available: <http://ebusiness.mit.edu/research/papers/133%20von%20hippel%20OSS%20innovation.pdf>.
- [9] D. Ehls, Joining decisions in open collaborative innovation communities: A discrete

choice study. Springer Science & Business Media, 2013.

[10] H. Yuan and B. He, "Brain-Computer Interfaces Using Sensorimotor Rhythms: Current State and Future Perspectives," (in eng), IEEE Transactions on Biomedical Engineering, vol. 61, no. 5, pp. 1425-35, May 2014.

[11] J. Malmivuo and R. Plonsey, Bioelectromagnetism - Principles and Applications of Bioelectric and Biomagnetic Fields. 1995.

[12] Standard Consumer Safety Specification for Toy Safety, 2018.

[13] DIRECTIVE 2014/53/EU OF THE EUROPEAN PARLIAMENT AND OF THE COUNCIL of 16 April 2014 on the harmonisation of the laws of the Member States relating to the making available on the market of radio equipment and repealing Directive 1999/5/EC, 2018.

[14] NeuroSky. The Force Trainer II: Hologram Experience. Available: <https://images-na.ssl-images-amazon.com/images/I/A1AOlb0qV1L.pdf>

[15] IEC 60601-1:2005+A1:2012(E), 2012.

[16] Apache License, Version 2.0, T. A. S. Foundation, 2004.

[17] U. X. Chaudhary, B. Silvoni, S. Cohen, LG. Birbaumer, N., "Brain-Computer Interface-Based Communication in the Completely Locked-In State," PLoS Biol, vol. 15, no. 1, 2018.

[18] L. F. Nicolas-Alonso and J. Gomez-Gil, "Brain Computer Interfaces, a Review," (in eng), Sensors (Basel), vol. 12, no. 2, pp. 1211-79, 2012.

[19] H.-J. Hwang, J.-H. Lim, Y.-J. Jung, H. Choi, S. W. Lee, and C.-H. Im, "Development of an SSVEP-based BCI spelling system adopting a QWERTY-style LED keyboard," Journal of

Neuroscience Methods, vol. 208, no. 1, pp. 59-65, 2012/06/30/ 2012.

[20] J. J. Vidal, "Toward Direct Brain-Computer Communication," Annual Review of Biophysics and Bioengineering, vol. 2, no. 1, pp. 157-180, 1973.

[21] K. Medical. (2018). Rhythmlink Deep Cup Dome Electrodes. Available: <https://kandel.com.br/eletrodos/eeg/deep-cup/>

[22] G. Technologies. (2018). g.SAHARAElectrode (16mm) Active Dry Electrodes. Available: <http://www.gtec.at/Products/Electrodes-and-Sensors/g.Electrodes-Specs-Features>

[23] J. Saab, B. Battes, and M. Grosse-Wentrup, "Simultaneous EEG Recordings with Dry and Wet Electrodes in Motor-Imagery," presented at the 12th Conference of Junior Neuroscientists of Tübingen, Heiligkreuztal, Germany., 2011/10, 2011. Available: <http://mlin.kyb.tuebingen.mpg.de/BCI2011JS.pdf>

[24] Bio-Medical. (2018). Electrodes for EMG|EEG|ECG|EKG. Available: <https://bio-medical.com/supplies/electrodes.html>

[25] g. t. M. Engineering. (2018). Comparision: active versus passive electrodes. Available: <http://www.gtec.at/News-Events/Newsletter/Newsletter-September-2010-Volume-29/articles/Comparision-active-versus-passive-electrodes2>

[26] P. A. Abhang, B. W. Gawali, and S. C. Mehrotra, "Chapter 1 - Introduction to Emotion, Electroencephalography, and Speech Processing," in Introduction to EEG- and Speech-Based Emotion Recognition, P. A. Abhang, B. W. Gawali, and S. C. Mehrotra, Eds.: Academic Press, 2016, pp. 1-17.

[27] A. M. Norcia, L. G. Appelbaum, J. M. Ales, B. R. Cottreau, and B. Rossion, "The steady-state visual evoked potential in vision research: A review," (in eng), Journal of Vision, vol. 15, no. 6, 2015.

[28] S. P. Kelly, E. C. Lalor, C. Finucane, G. McDarby, and R. B. Reilly, "Visual spatial

attention control in an independent brain-computer interface," IEEE Transactions on Biomedical Engineering, vol. 52, no. 9, pp. 1588-1596, 2005.

[29] L. Zhang, X. j. Guo, X. p. Wu, and B. y. Zhou, "Low-cost circuit design of EEG signal acquisition for the brain-computer interface system," in 2013 6th International Conference on Biomedical Engineering and Informatics, 2013, pp. 245-250.

[30] M. Leonardo Casal and Guillermo La, "Skin-electrode impedance measurement during ECG acquisition: method's validation," Journal of Physics: Conference Series, vol. 705, no. 1, p. 012006, 2016.

[31] M. Jansen et al., "Motion-related artefacts in EEG predict neuronally plausible patterns of activation in fMRI data," Neuroimage, vol. 59, no. 1-3, pp. 261-270, 02/23/received

[32] A. B. Usakli and S. Gurkan, "Design of a Novel Efficient Human-Computer Interface: An Electrooculogram Based Virtual Keyboard," IEEE Transactions on Instrumentation and Measurement, vol. 59, no. 8, pp. 2099-2108, 2010.

[33] A. B. Usakli, "Improvement of EEG Signal Acquisition: An Electrical Aspect for State of the Art of Front End," Computational Intelligence and Neuroscience, vol. 2010, 2010.

[34] B. Fong, M. Harvey, and K. Lagoutchev "Portable EEG Recording Using a Lock-in Amplifier," Electrical And Computer Engineering, University of Illinois, 2014.

[35] B. Luan, M. Sun, and W. Jia, "Portable Amplifier Design for a Novel EEG Monitor in Point-of-Care Applications," Proceedings of the IEEE ... annual Northeast Bioengineering Conference. IEEE Northeast Bioengineering Conference, vol. 2012, pp. 388-389, 2012.

[36] T. Instruments. (2018). Three guidelines for designing anti-aliasing filters - Precision Hub - Archives - TI E2E Community. Available:

https://e2e.ti.com/blogs_/archives/b/precisionhub/archive/2015/11/06/three-guidelines-for-designing-anti-aliasing-filters

[37] M. Buttlar, J. Hansmann, and A. R. The ModularEEG. Available:

<http://openeeg.sourceforge.net/doc/modeeg/modEEGamp-v1.0.png>

- [38] B. B. Winter and J. G. Webster, "Driven-right-leg circuit design," IEEE Transactions on Biomedical Engineering, vol. BME-30, no. 1, pp. 62-66, 1983.
- [39] M. R. Ahsan, M. Ibrahimy, and O. Khalifa, EMG Signal Classification for Human Computer Interaction A Review. 2009, pp. 480-501.
- [40] R. Saji, K. Hirasawa, M. Ito, S. Kusuda, Y. Konishi, and G. Taga, "Probability distributions of the electroencephalogram envelope of preterm infants," Clinical Neurophysiology, vol. 126, no. 6, pp. 1132-1140, 2015/06/01/ 2015.
- [41] Andrew. (2013). Fitting a Model by Maximum Likelihood. Available: <https://www.r-bloggers.com/fitting-a-model-by-maximum-likelihood/>
- [42] Quantivity. (2011). Why Minimize Negative Log Likelihood? Available: <https://quantivity.wordpress.com/2011/05/23/why-minimize-negative-log-likelihood/>
- [43] K. P. Murphy, "Naive bayes classifiers," University of British Columbia, vol. 18, 2006.
- [44] Botland. (2018). STM32 NUCLEO-F303K8 - STM32F303K8 ARM Cortex M4. Available: <https://botland.com.pl/stm32-nucleo/4891-stm32-nucleo-f303k8-stm32f303k8-arm-cortex-m4.html>
- [45] Amazon. BITSCOPE MP01A BNC ADAPTER, MICRO OSCILLOSCOPE. Available: <https://www.amazon.com/BITSCOPE-MP01A-ADAPTER-MICROOSCILLOSCOPE/dp/B01E9QZYBA>
- [46] M. M. Equipment. (2018). Technomed Reusable EEG Cup Electrode (12/Pkg). Available: <https://mfimedical.com/products/technomed-reusable-eeeg-cup-electrode>
- [47] T. S. Physiologist. (2015). The ECG Leads, Polarity and Einthoven's Triangle. Available: <https://thephysiologist.org/study-materials/the-ecg-leads-polarity-and-einthovens-triangle/>
- [48] H. R. Warner. (2018). Measure ECG and arrhythmia detection. Available: <http://www.hrwproject.com/ecg.html>

